Department of Physics and Astronomy

University of Heidelberg

Bachelor thesis

in Physics

submitted by

Daniel Winkler

born in Friedrichshafen

2018

Characterization of a HPGe Coaxial Well Detector for Low Energy Gamma Spectroscopy

&

Sensitivity Analysis of Germanium Spectrometers

This Bachelor thesis has been carried out by Daniel Winkler

at the

Max-Planck-Institut for Nuclear Physics

under the supervision of

Herrn Prof. Dr. Dr. h.c. Manfred Lindner

Charakterisierung eines HPGe Bohrloch Detektors für niederenergetische Gammaspektroskopie & Sensitivitätsvergleich von Germaniumspektrometern:

Auf der Suche nach physikalischen Phänomenen jenseits des Standardmodells ist es für Experimente mit seltenen Ereignissen unerlässlich den radioaktiven Untergrund der Umgebung zu reduzieren. Die Auswahl möglichst strahlungsfreier Materialien ist eine wesentliche Voraussetzung, um eine niedrige radioaktive Verunreinigung im Detektoraufbau sicherzustellen. In vielen Fällen kann dies mit "Low-Level" Gamma-Spektroskopie erreicht werden. Für die Analyse und die Aktivitätsbestimmung der vermessenen Proben, ist eine genaue Kenntnis der Spektrometereigenschaften notwendig.
Diese Arbeit ist der erste Schritt für die Wiederinbetriebnahme eines Bohrloch Spektrometers, welches speziell für Niederenergie Gamma-Spektroskopie entwickelt wurde. Die Geometrie des Detektors wurde in einer Monte Carlo Simulation implementiert. Charakteristische Parameter, wie die Totschichtdicke und die Dicke der Spektrometerendkappe wurden über einen Vergleich von Simulation und Messung bestimmt. Das entwickelte Software Model wurde dann genutzt um den Einfluss verschiedener Untergrundbeiträge und deren Reduktion mit geeigneter Abschirmung abzuschätzen.
Im zweiten Teil der Arbeit wird eine Sensitvitätsstudie für Germaniumspektrometer behandelt. Dabei werden fünf verschiedene Detektoren mit einem standardisierten Verfahren verglichen. Dieses ermöglicht es, den Vergleich für weitere Detektoraufbauten anzuwenden.

Characterization of a HPGe Coaxial Well Detector for Low Energy Gamma Spectroscopy & Sensitivity Analysis of Germanium Spectrometers:

Experiments looking for phenomena beyond the standard model substantially rely on environmental background reduction. Therefore, it is crucial to any of these experiments to conduct a precise material selection in order to ensure high radiopurity near the detector volume. In many cases, this can be achieved by low-level gamma-spectroscopy. Detailed knowledge of the characteristics of the spectrometers is required to determine the activity of a sample.
Within this thesis, a coax well spectrometer, designed for low energy gamma spectroscopy, has been reactivated. The geometry of the detector was implemented in a Monte Carlo simulation. Characteristic parameters of the spectrometer such as the dead layer thickness and the thickness of the end cap were determined by matching the simulation to the measurement. The implemented software model was then used to estimate the different background contributions and their expected reduction due to dedicated shielding.
The second part of this work addresses the sensitivity determination of germanium spectrometers. A study with five different detectors was performed with a standardized procedure, making it possible to compare different detector setups.

Contents

I Low Level Gamma Spectroscopy 1

1 Introduction 1

2 Gamma radiation 1
2.1 Origin of gamma radiation 1
2.2 Interaction of gamma radiation with matter 2
2.3 Detection of gamma radiation with germanium spectrometers 4
2.4 Analysis of gamma spectra 6

3 Radioactive background 7
3.1 Natural radioactivity 7
3.2 Man-made contaminations 8
3.3 Cosmic rays 8

II Sensitivity Comparison of Germanium-Spectrometers 11

1 Motivation 11

2 Procedure 11
2.1 General definitions 11
2.2 Analysis 12

3 Results 15

4 Conclusion 17

III Characterization of a Coaxial Well Gamma Spectrometer 19

1 Motivation 19

2 General description of the detector & Commissioning 19
2.1 Coaxial well type & Crystal parameters 19
2.2 Internal structure & End cap 20
2.3 DAQ & Detector operation 21

3 Implementation & Optimization of the software model 21
3.1 Basic implementation 21
3.2 Determination of the dead layer thickness 23
3.3 Estimation of the end cap thickness inside the borehole & the front . 29

3.4 Active volume adjustment 32

4 Estimation of the influence of different background components 33
4.1 Background measurement 33
4.2 Background of the environment 34
4.3 Muon induced background 35
4.4 Background due to impurities in the lead shielding 38

5 Simulation & Measurement of a ^{210}Pb source 39

6 Results & Discussion 41

7 Outlook 41

Appendix 43

References 45

Part I
Low Level Gamma Spectroscopy

1 Introduction

The standard model and its predictions have been confirmed by many physics experiments. However, numerous experimental indications and theoretical considerations suggest, that it is not a comprehensive description of the elemental particles. Evidence like the neutrino mass or the existence of dark matter indicates that this model is not complete.
To investigate the physics beyond the standard model, experiments searching for rare events are performed. These are, e.g., the direct detection of dark matter in the form of WIMPs (Weakly Interacting Massive Particles), as sought in the XENON1T experiment [1] or the proof of the neutrinoless double beta decay in the GERDA experiment [2]. Due to the rare occurrence (low cross-section) of the desired events, the detection is a challenge and the reduction of the radioactive background is of primary importance for those experiments. Thereby, low-level gamma spectroscopy is an important tool.
The main purpose of the low-level gamma ray spectroscopy performed at the Max-Planck Institute für Kernphysik is the investigation of the radiopurity of materials. Measured samples are mostly candidates for the construction materials to be used in the mentioned experiments searching for rare events.

2 Gamma radiation

First, the origin of gamma radiation and its interaction with matter are illustrated in a very general manner. Afterward, the operating principle of gamma spectrometer and the basic analysis of gamma energy peaks are described.

2.1 Origin of gamma radiation

Radioactive radiation can be divided into three types: alpha-, beta & gamma-radiation. All types are caused by unstable atoms, which have an excess of energy. In order to reach a stable state, that extra energy has to be released in the form of radiation. Alpha- and beta-radiation are emitted by a nuclear disintegration process, changing the number or type of nucleons in the nucleus. The resulting daughter nucleus is usually left in an excited state. It can then de-excite to a lower energy state by emitting a gamma ray, called gamma decay. Gamma radiation is therefore solely the losing of surplus excitation energy and usually a by-product of alpha or beta decay. The resulting radiation is monoenergetic and characterizes most of the time the emitting nucleus explicitly. On the basis of a gamma spectrum, the present isotope and its quantity can be identified.

2.2 Interaction of gamma radiation with matter

The instrumental detection of any particle or radiation often depends upon the production of charged secondary particles which can be collected to produce an electrical signal. Since photons are uncharged, gamma ray detection depends upon other types of interaction which transfer the gamma energy to electrons within the detector material. In the following the processes that occur if gamma radiation penetrates the detector material are described. These depend on both the energy of the radiation, as well as the mass number of the absorber material. Thereby, the attenuation coefficient is of central importance. It describes the extent to which the radiant flux of a beam is reduced as it passes through a specific material. In general, the attenuation increases with higher mass number, which is the reason why materials with a high mass number are used for the detector parts and its shielding (see Fig. 1). The following considerations are essentially taken from [3, 4].

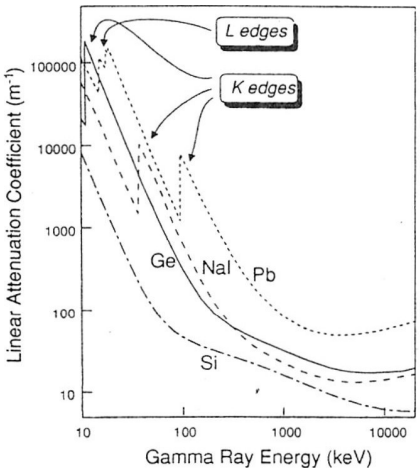

Figure 1: Attenuation coefficient of materials as a function of gamma energy [3]

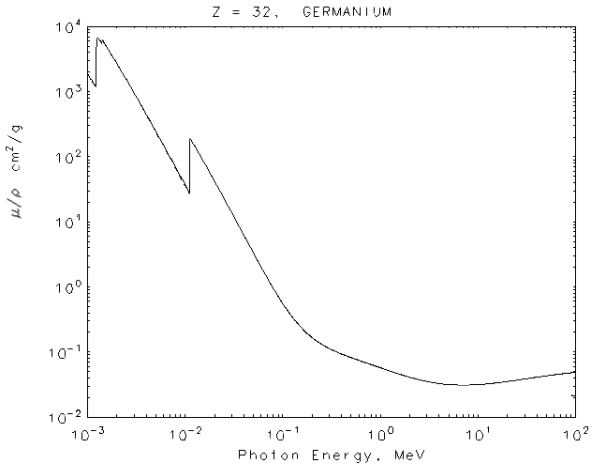

Figure 2: Mass-attenuation coefficient of gamma radiation in germanium as a function of the gamma energy [5]

The curve in Fig. 2 is the sum of the interactions via photoelectric absorption, Compton scattering, and pair production.
In the low energy range (10 keV to 500 keV) the photo effect is dominating. It arises by the interaction of a gamma with one of the bound electrons in an atom, which is ejected from its shell. Its kinetic energy is then given by the gamma energy reduced by the binding energy. Due to the released binding energy, the atom remains in an excited state. The excess energy can be redistributed to other electrons of the atom, which can result in the release of further electrons from the atom (Auger cascade). Alternatively, the vacancy in the electron shell may be filled by a higher energy electron falling into the lower energy state and thereby emitting characteristic X-rays (X-ray fluorescence). This may result in further photoelectric absorption. The en-

ergy level from which the electron is ejected depends upon the energy of the incident gamma and leads to discontinuities in the curve of the attenuation coefficient. This can be seen for the case of germanium in Fig. 2 at 11.1 keV. Below this value, only electrons from the L-shell or higher can be ejected, while above also the ejection from the K-shell is possible, which prompt the sudden rise of the attenuation coefficient. These edges appear at the binding energies and correspond to the electron shells.
For larger gamma energies (100 keV to 1000 keV), Compton scattering contributes significantly to the energy deposition of the gamma radiation in the detector material. Compton scattering is a direct interaction of the photon with the electron, where the photon scatters and transfers a part of its energy to the electron. The scattered photon has consequently an increased wavelength. The energy imparted to the recoil electron is depended on the scattering angle and maximal for 180° (back-scattering) ($\hat{=}$ Compton edge), but always less than the total gamma energy. The Compton continuum is therefore always below of the full energy peak. The scattering with bound electrons and the finite detector resolution lead to a rounding of the Compton edge as seen in Fig. 3 left.
In the high energy range (>1022 keV) pair production gets relevant. The photon interacts with the Coulomb field of the nucleus, resulting in the conversion of the gamma into an electron-positron pair. Hence the gamma energy has to be at least equivalent to two times the rest mass of the electron (1022 keV). After the positron loses energy and thermalizes, it annihilates with an electron and produces two photons, which are emitted into opposite directions (momentum conservation). Their energy deposition results in an annihilation peak in the spectrum, which is due to the Doppler broadening wider than a typical gamma peak.
All these processes occur in the detector and enable the detection of gamma radiation. Since the detector size is finite some photons can escape the detection. For example, one or both photons could escape the detector after the annihilation, resulting in a single- or double escape peak. Moreover, a photon can undergo multiple Compton scattering and leave the detector without depositing its entire energy, which results in the Compton continuum below the full energy peak. These and other effects generate the typical gamma ray spectrum shown in Fig. 3 right.

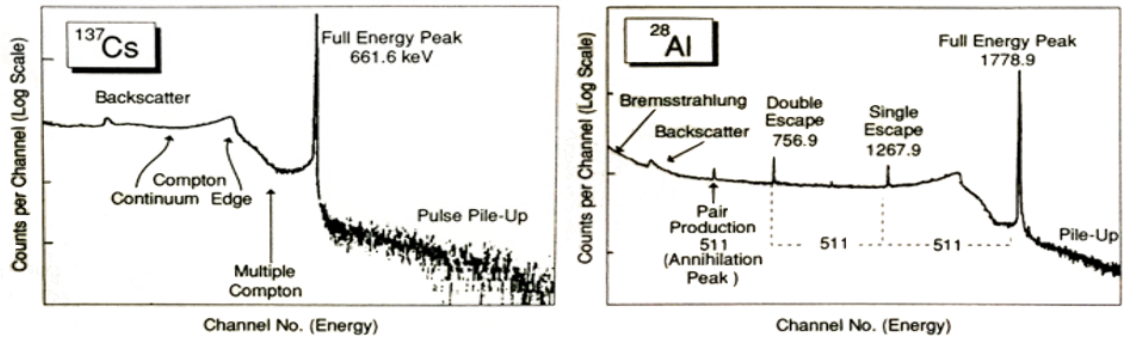

Figure 3: Example spectra, illustrating the various features of the interaction of gamma radiation with the detector [3].

2.3 Detection of gamma radiation with germanium spectrometers

The combination of their high density and the small energy required to create an electron-hole pair (2.96 eV in Ge), makes semiconductors useful materials for spectrometry of ionizing radiation [6]. Semiconductor detectors make use of the small energy gap between the valence and conduction bands of the semiconductors (0.67 eV in Ge). At low temperatures, most electrons are confined to the valence band. By adding energy to the electron (e.g. by interaction with ionizing radiation), it is raised into the conduction band, where it can move freely in the crystal. After the electron's transfer into the conduction band, a positively charged ion is left at its place. If an electric potential is applied, current flows by conduction band electrons and also by movement of the positive charges called holes. For a more detail description of the band structure see [3, 7].
To increase the number of free charge carriers, semiconductors can be doped by introducing foreign atoms with a different number of valence electrons into the lattice. Acceptor atoms are impurities with one electron less in their valence band (e.g. boron). Placed inside a semiconductor crystal, this electron is missing in the covalent bond with the semiconductor atoms. An electron can be attracted to this covalent bond, thus a hole is created and can conduct current. The positively charged current of the holes is then dominating and one refers to a p-type semiconductor. Conversely, donor impurities (e.g. lithium) have an extra electron, which is easily released into the conduction band. These are called n-type semiconductors.
To detect gamma radiation in the semiconductor, it is necessary to remove all free charge carriers from the material, otherwise the fluctuations in the current created by them could overwhelm the signal from the radiation interactions. This can be accomplished by joining p- and n-type semiconductors. An area devoid of free charges is created at the junction, called the depletion region [7]. This is due to the free electrons of the n-type diffuse into the p-type material and holes vice versa. Charged immobile ions are left at the filled acceptor sites and vacated donor sites. A space charge suppressing further charge carrier diffusion is created and a potential difference builds up across the junction. The arising electric field will then force any electron or holes created in this region to drift towards the positive or negative potential, respectively.
This way an electric signal will be generated at the borders of the junction and the depleted region acts as a sensitive volume of the detector. However, due to the small gap between the valence and conductive band, thermal excitation can cause charge carriers to appear in the conduction band and thus a small leakage current results. To sufficiently deplete the p-n junction, it is therefore necessary to cool the diode to cryogenic temperatures.
The electric field inside the depleted region and consequently the region's width can be significantly increased by augmenting the potential difference across the p-n junction with an externally applied voltage. This external voltage is called reverse bias because the potential difference is applied in the direction in which no current can flow across the diode [8].

The primary electrons (with energies considerably greater than thermal energies) produced by incident gamma radiation trigger additional charge carriers. Interactions of the primary electrons can raise other electrons in to the conduction band and a cascade of electron-hole pairs for each primary electron arises. The number of produced charge carriers is proportional to the gamma energy. In total $N = \frac{E_\gamma}{\epsilon}$ electron-hole pairs are created, where ϵ is the average energy to create an electron-hole pair in germanium. The charge is collected via the electric field and a signal in form of a pulse whose height is proportional to the gamma energy is produced. These pulses are amplified and fed into a multi-channel analyzer (MCA) and the gamma spectrum is recorded. A more detailed description of the relevant electronics can be found in [3].
In practice, germanium spectrometers are not constructed by placing different types of semiconductors in contact but by conversion of one face of a block of germanium to the opposite type by evaporation and diffusion or by ion implantation [3]. This way a depletion layer throughout the crystal is created. The germanium material can be either n- or p-type, depending on the concentration of donor or acceptor atoms in the crystal. To connect the diode to an electrical circuit, contacts to the crystal are needed. These electrical contacts on the crystal (in the case of a p-type) are a thick lithium contact (n^+-contact), which also produces the junction, and a thin ion (boron) implanted contact which is the p^+-contact (the + indicates thereby a strong doping). The crystal can be cut or ground to any shape. However, the electrical field inside the crystal is very important, which limits the useful shapes to a disk or a cylinder with a hollow core. A typical coaxial p-type detector is shown in Fig. 4.

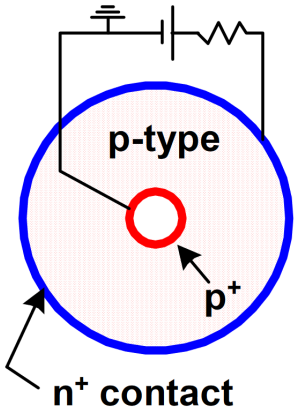

Figure 4: Electrode configuration for p-type coaxial detector [9]

The areas outside the depletion region, where lithium and boron were diffused are not sensitive for gamma radiation. These areas are the so called dead layers. The dead layer itself represents a plane that has to be passed by gamma radiation before reaching the active volume in the crystal. Interactions in the dead layer will lead to an incomplete charge collection because of the very weak electric field in this region. Therefore, events generated there yield no pulse.

2.4 Analysis of gamma spectra

The aim of material investigations is the identification of the radioactive components and their specific activities. The specific activity is given by

$$A_\gamma = \frac{N}{m \cdot \epsilon_D \cdot \beta_{BR} \cdot t} \quad , \tag{1}$$

and the relative error by

$$\frac{\Delta A_\gamma}{A_\gamma} = \sqrt{\left(\frac{\Delta N}{N}\right)^2 + \left(\frac{\Delta t}{t}\right)^2 + \left(\frac{\Delta \epsilon_D}{\epsilon_D}\right)^2 + \left(\frac{\Delta \beta_{BR}}{\beta_{BR}}\right)^2 + \left(\frac{\Delta m}{m}\right)^2} \quad , \tag{2}$$

where m is the mass of the sample, t the measurement time and N the number of counts. ϵ_D is the detection efficiency, which describes the possible signal yield. The detector takes only a finite solid angle relative to the sample. Therefore, only a certain proportion of the emitted gammas can reach the detectors active volume and deposit energy. Ultimately, the efficiency depends on the placement, geometry and the self-absorption properties of the sample, as well as the geometry of the detector. To determine the efficiency, a simulation model of the detector is required. β_{BR} is the branching ratio of the gamma line under investigation and represents the probability of the radiation of a gamma of a certain energy.

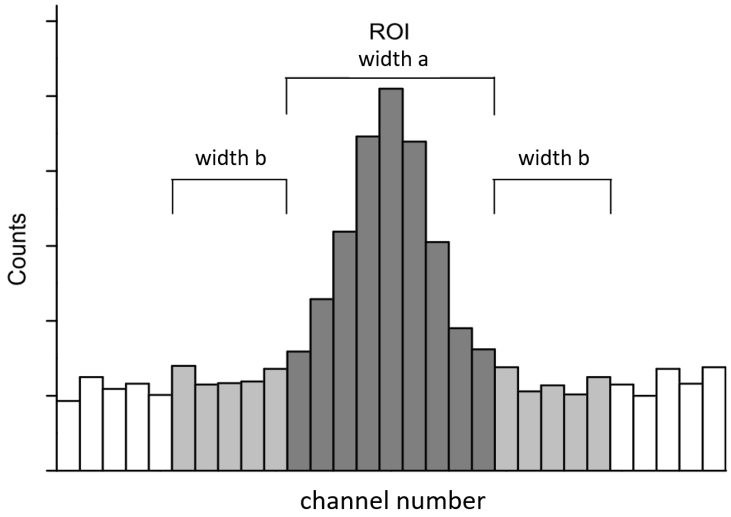

Figure 5: Region of interest (ROI) and background zones of a typical gamma peak

After completion of the measurement, the obtained gamma spectrum is analyzed to extract the counts N of the relevant peaks. For this, one can use the norm DIN 25482-5 for gamma spectroscopic investigations. The region of interest (ROI) is defined as $2.5 \cdot$ FWHM (full width half maximum) around the center of the peak. The width of the ROI is labeled as a. The integral count rate of this region is given

by N_{ROI}. To take the continuous background into account, one specifies regions left (width b^{left}) and right (width b^{right}) to the ROI. Usually, the width of these intervals on each side is half the width of the ROI ($b^{left} = b^{right} = \frac{a}{2}$). N_{BKG}^{left} and N_{BKG}^{right} are the integral count rates in these regions. An illustration of these regions is shown in Fig. 5, [10]. By applying a background correction, the counts in the peak are given by

$$N = N_{ROI} - \frac{N_{BKG}^{left} + N_{BKG}^{right}}{b^{left} + b^{right}} \cdot a \quad . \tag{3}$$

3 Radioactive background

The radioactive background interferes with experiments having low count rates. In order to effectively suppress the background, the different components and their origin have to be known. Gamma radiation of natural radioactivity or cosmic rays contribute significantly to the background. In the following, an overview of the most important background components is given. A detailed description of the background components and their significance for the low-level spectroscopy can be found in [11].

3.1 Natural radioactivity

Nearly all common materials contain a certain radioactive contamination due to the primordial decay isotopes ^{232}Th, ^{238}U and ^{40}K with half-lives of several billions of years [12]. The isotopes produced in those decay chains (see Fig. 7) are also radioactive and pose a strong background source in germanium spectroscopy and in general for rare event experiments. The most energetic gamma ray line by natural radioactivity (2.6 MeV) is emitted by ^{208}Tl, a daughter nucleus of the ^{232}Th decay chain. Relevant isotopes are also ^{214}Bi (^{238}U decay chain) and the decay daughters originating from radon (several isotopes). Radon contaminations are particularly problematic for low-level gamma spectroscopy since radon as a noble gas can easily diffuse through walls and shields and thus get directly to the detector. Ventilation of the experimental area is required to avoid accumulations around the detector.
To suppress the background originating from natural radioactivity a suitable shielding is required. For example 15 cm to 20 cm of lead is enough to suppress this background effectively [11]. As a product of the ^{226}Ra decay series, the isotope ^{210}Pb found in lead is a critical factor. The strong β-radiation of its decay daughter ^{210}Bi results in a continuous bremsstrahlung and characteristic X-ray spectrum in lead. As a consequence, attention must be paid in selecting the materials brought for shielding into the vicinity of the detector. A low radioactive contamination of these materials is essential. This is checked in material screening.

3.2 Man-made contaminations

Besides natural radioactivity, there are man-made contaminations in the environment. Nuclear weapon test or the Chernobyl disaster produced isotopes like ^{137}Cs that can be found in the atmosphere [11]. Another example would be the use of certain isotopes in production processes, e.g. ^{60}Co is used in the production of steel [11].

3.3 Cosmic rays

Another significant source of background is the secondary radiation of cosmic rays. It arises by the interaction of the cosmic primary radiation, which mostly consists of protons and helium nuclei, with the nitrogen or oxygen molecules present in the earth's atmosphere. This creates particle showers, the secondary radiation. At the end of long decay chains, mainly electrons, positrons, neutrons, protons, pions and muons remain at sea level. While the other components of the cosmic secondary radiation are very effectively suppressed by a shielding of massive soil, the muon flux is barely reduced (see Fig. 6). To reduce the muon flux significantly several thousand meters of overburden are needed. The muons reaching the detector contribute to the background e.g. by ionization of the diode or by secondary reactions with the shielding material, producing, e.g., neutrons.

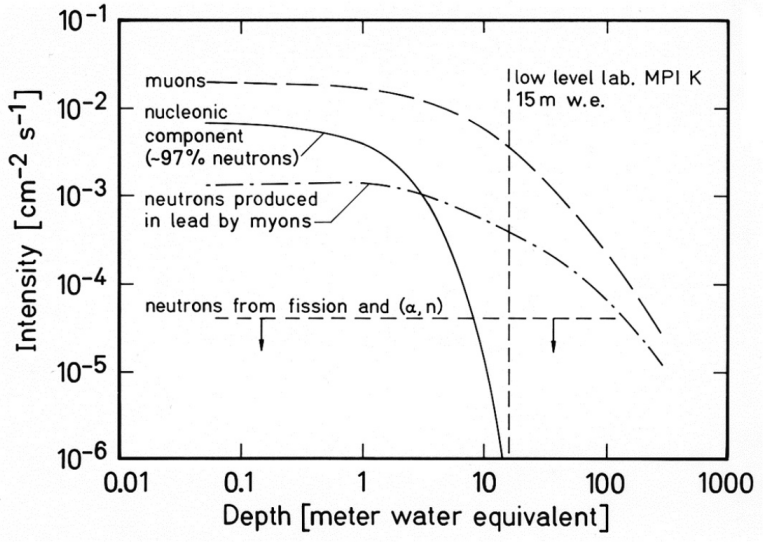

Figure 6: Reduction of the muon flux and others components of the secondary cosmic radiation with increasing laboratory depth [13].

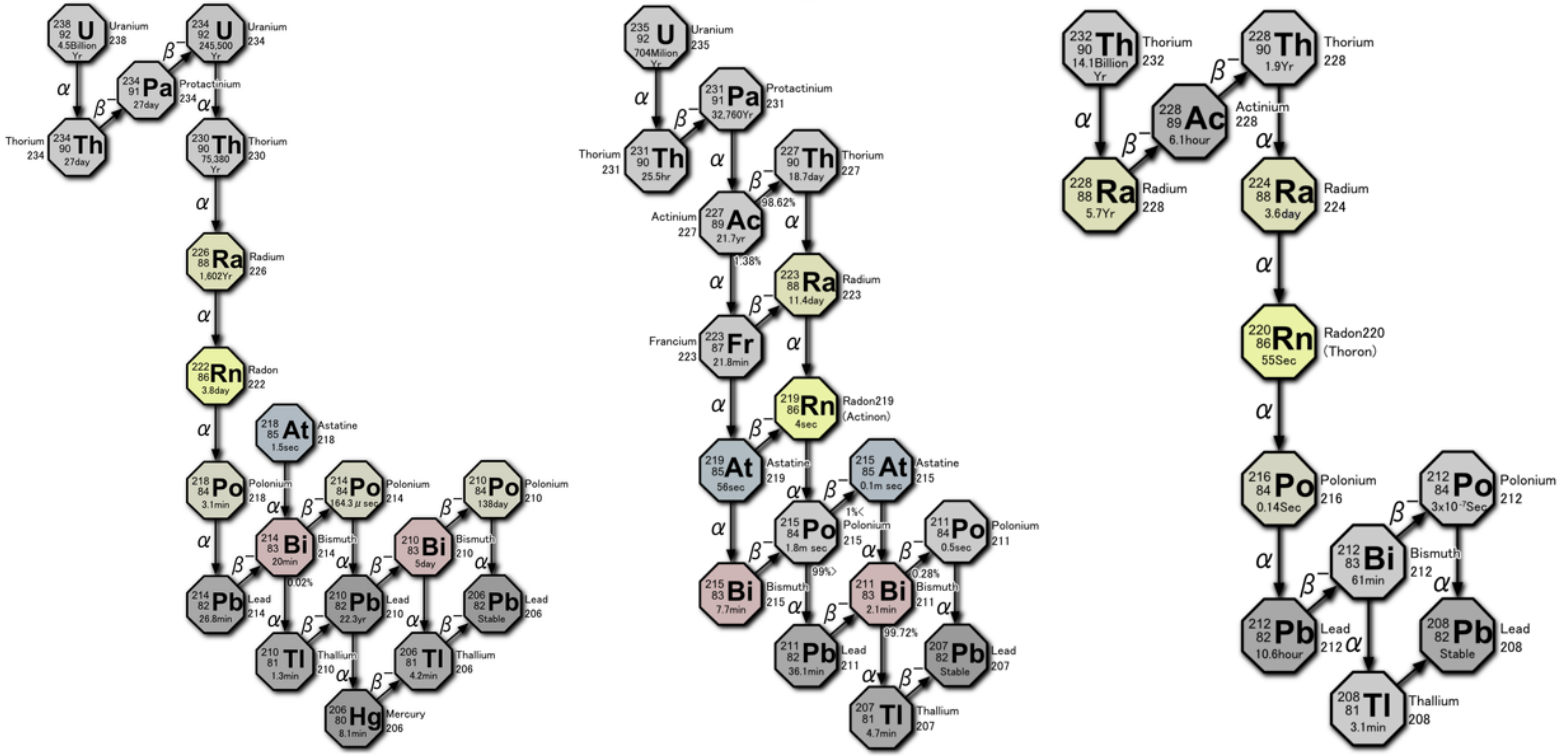

Figure 7: Decay chains of ^{238}U & ^{235}U & ^{232}Th [14]

Part II
Sensitivity Comparison of Germanium-Spectrometers

1 Motivation

State of the art germanium spectrometers push their sensitivities to the lowest possible limits and thereby detect the smallest activity concentrations of primordial, anthropogenic and cosmogenic decay isotopes in materials. In order to compare their performance in detecting radioactive trace impurities a uniform benchmark is required. The utilized procedure presented in this chapter describes how to obtain a threshold activity for these isotopes. The threshold activity is a characteristic limit, which, when exceeded by a measurement, can be used to claim the presence of an element or radionuclide in the sample at a certain confidence.
In this study five gamma spectrometers are analyzed. Three of them are located in the low-level laboratory (LLL) at the Max-Planck Institut für Kernphysik in Heidelberg (Bruno, Corrado [15], GIOVE [16]), one is installed in an underground laboratory in Switzerland (GeMSE [17]), while the last one is operated at the Gran Sasso underground laboratory (LNGS) in Italy (GEMPI II [18]). The LLL is at shallow depth with a water equivalent of ∼15 m, the laboratory in Switzerland of ∼620 m, while the massive rock layer in Gran Sasso has a water equivalent of ∼3400 m.

2 Procedure

2.1 General definitions

To obtain a threshold activity, the decision threshold (DT) is calculated first and then converted into a threshold activity. The following procedure is based on the descriptions in [10, 16, 19].
The decision threshold is defined as the critical value of a statistical test of the null-hypothesis ($\eta = 0$) versus the alternative hypothesis ($\eta > 0$). It allows a decision to be made for a measurement y on whether or not, for instance, radiation of a possibly radioactive sample is present. The critical value is defined by

$$P(y > DT|\eta = 0) = \alpha \quad , \tag{4}$$

where P is the probability density function of the measurement y with unknown true value η (here estimated to be zero (null-hypothesis)). α is a chosen probability, representing the confidence limit of the test. In good approximation P is normally distributed with standard deviation Δy [10]. Fig. 8 illustrates the definition of the decision threshold. One can deduce

$$DT = k_\alpha \cdot \sigma = k_\alpha \cdot \Delta y(0) \quad , \tag{5}$$

where k_α is the coverage factor representing the chosen confidence limit and $\Delta y(0)$ labels the standard deviation around 0.

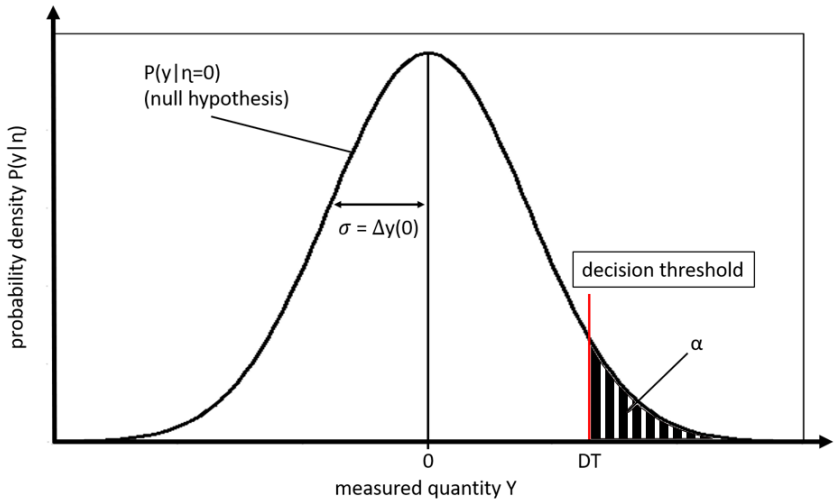

Figure 8: Illustration of the decision threshold for the null-hypothesis. The shaded area above the decision threshold represents the range where the null-hypothesis should be rejected.

In a measurement two cases can occur:

- $y > DT$: The measurement exceeds the decision threshold. The null-hypothesis is rejected with a probability of $1-\alpha$. The alternative hypothesis applies and one can conclude that a radionuclide is present in the sample.

- $y \leq DT$: The null hypothesis cannot be rejected. The measurement is compatible with the background and one can conclude that a radionuclide is not present in the sample.

A wrong rejection of the null-hypothesis is called error of the first kind, which happens with the probability α.

2.2 Analysis

To determine the decision threshold for the analysis of the sensitivity, the background spectra of the different detectors have to be evaluated. The measurands in gamma spectroscopy are the counts of a certain gamma energy line originating from the decay of a radioactive isotope. For this study, the sensitivities for the isotopes shown in Tab. 1 are analyzed. Subchain denotes a higher mother nuclide of the shown isotopes, which itself is part of e.g. the Th-chain. The emitted gamma ray lines are then associated with the subchain isotope.

Subchain	Isotope	Energy [keV]	Subchain	Isotope	Energy [keV]
^{226}Ra	^{214}Pb	295.2	^{228}Ra	^{228}Ac	969.6
	^{214}Pb	351.9		^{228}Ac	911.20
	^{214}Bi	609.3	^{228}Th	^{208}Tl	583.2
	^{214}Bi	1120.3		^{208}Tl	2614.5
	^{214}Bi	1764.5	^{60}Co	^{60}Co	1173.2
^{238}U	^{234m}Pa	1001.0		^{60}Co	1332.5
^{40}K	^{40}K	1460.8	^{137}Cs	^{137}Cs	661.7

Table 1: Overview of the investigated radioactive isotopes and the corresponding gamma ray energies in the analysis of the sensitivity

One defines a region of interest (ROI) (Sec. I.2.4) at the positions of the gamma ray lines i belonging to the subchain under investigation. The net counts y of a gamma ray line are obtained by

$$y = N - N_{Bkg} \quad , \tag{6}$$

$$\Delta y = \sqrt{\Delta N^2 + \Delta N_{Bkg}^2} \quad ,$$

where N are the counts in the region of interest (ROI) and N_{Bkg} are the according counts of the background. The standard deviation is obtained by Gaussian error propagation. Using $\Delta N = \sqrt{N}$ in eq. 6 one obtains

$$\Delta y(y) = \sqrt{y + N_{Bkg} + \Delta N_{Bkg}^2} \quad . \tag{7}$$

As previously mentioned, one assumes the null-hypothesis to determine the decision threshold. The null-hypothesis implies there is no contribution from the source ($y = 0$). The expectation value of the measured counts N is therefore equal to the expectation value of the background counts N_{Bkg}. Consequently, the recorded events in the matching region of interest are then considered as the expectation value for the background contribution in a sample measurement

$$\Delta y(0) = \sqrt{N_{Bkg} + \Delta N_{Bkg}^2} = \sqrt{2 \cdot N_{Bkg}} \quad . \tag{8}$$

The decision threshold is then defined as

$$DT_i = k_\alpha \cdot \sigma_i = k_\alpha \cdot \sqrt{N_i + \Delta N_i^2} = k_\alpha \cdot \sqrt{2N_i} \quad , \tag{9}$$

where the index i implies a certain gamma ray line. N_i are the counts in the corresponding ROI in the background measurement and ΔN_i the respective error. k_α is the coverage factor. In the following, $k_\alpha = 1.645$ is chosen, corresponding to a 95% C.L. or 5% error of the first kind.
Evidently, the achievable sensitivity depends on the counting time of the background measurement. In order to get a comparable result for different measuring times, the counts N are normalized to a typical standard counting time of 30 days.
The next step is to convert the numerical value of the decision threshold into a threshold activity. By using the detection efficiency ϵ_D and the branching ratio ϵ_{BR} of the gamma ray line under investigation as well as the measurement time t of 30 days as previously mentioned.
To determine the detection efficiency or collection efficiency, respectively, i.e. the probability to detect the full absorption energy of gamma rays emitted from an external source position, the detector geometry and its shielding has to be implemented in a full Monte Carlo simulation. The simulation error in form of a relative error of the detector efficiency is taken into account in the above formula by $\Delta\epsilon_{D,rel}$. This simulation error is an estimate of the systematic uncertainty of the software model. It was obtained by optimizing the Monte Carlo model, for example, using calibrated sources all around the detector and comparing the data with simulations as done in [6] for Bruno & Corrado. One obtains

$$DT_i' = k_\alpha \cdot \frac{\sqrt{N + \Delta N^2 + (\Delta\epsilon_{D,rel} \cdot N)^2}}{\epsilon_D \cdot \epsilon_{BR} \cdot t} \quad . \tag{10}$$

Since the efficiency depends predominantly on placement, geometry and self-absorption attributes of the sample as well as of the surrounding materials, a general number cannot be given. For the benchmark sensitivity, two reference samples are considered to represent two extreme cases. First a point-source, which is placed centered in front of the detector cap to be as close as possible to the germanium crystal, to represent the small low-mass samples. The second case includes the large volume and high-density samples, which fill almost the entire sample chamber. They are represented by a copper block, which fills the sample chamber completely. The mass of the block is ∼9.05 kg for Bruno, ∼118.60 kg for Corrado, ∼93.85 kg for GIOVE, ∼118.86 kg for GeMPI II and ∼170.83 kg for GeMSE. In the resulting simulations of the two cases, the efficiency for each gamma energy line is computed as the ratio between the number of counts detected in the line and the number of gamma rays emitted at that energy in a total event count of 30 millions.
If the background for a sample chamber partly or completely filled with clean copper is even lower than for an empty chamber, the background spectrum with the filled chamber is used instead. The sensitivity for a large high-density sample is in such cases even better than if estimated from the empty background measurement. This is the case for GIOVE in a background measurement with a 62.5 kg copper filled chamber. If the background does not improve for copper or other chamber-filling

high-density samples, the empty background spectrum as described before is used. The threshold activities in mBq are then calculated for each gamma ray line. Additionally, the results for the second case of samples are normalized to the mass of the copper sample to get a threshold activity in mBq/kg.
In a next step the threshold activity for a subchain and therefore a combination of n lines is determined. The gamma ray lines belonging to the same subchain in radioactive equilibrium, are combined using the weighted average to get the combined threshold activity as the overall sensitivity

$$DT'_{com} = \sqrt{\frac{1}{\sum \frac{1}{DT_i'^2}}} = k_\alpha \cdot \sqrt{\frac{1}{\sum \frac{1}{\sigma_i^{*2}}}} \quad , \quad \sigma_i^* = \frac{\sigma_i}{\epsilon_D \cdot \epsilon_{BR} \cdot t} \quad . \tag{11}$$

This is a valid approach since the error calculation for the decision threshold and the modification to a threshold activity can be interchanged. The branching ratio ϵ_{BR} and the detection efficiency ϵ_D introduce additional weighting factors. t as a global variable does not make a difference. Thereby, gamma ray lines with a high total efficiency ($\epsilon_{tot} = \epsilon_{BR} \cdot \epsilon_D$) are weighted stronger, additionally to the weighting by the according background counts.

3 Results

In Fig. 9 the detection efficiencies for the investigated detectors are shown for the case of the point source, while Fig. 10 shows the case of the copper filled sample chamber. The efficiency is plotted as a function of the gamma energy.
For case one (Fig. 9) the overall shape for the different detectors is identical. The detection efficiency decreases towards higher energies as one would expect. The variation in magnitude is due to the different sizes of the crystals as well as the thickness of their dead layer. The apparent drops in the efficiency, e.g. at an energy of 583.19 keV, deviate from the expected continuous decrease. This is explained by summation effects. Since the detectors have a finite time resolution (typically nanoseconds), gamma rays which are emitted within such a short time range can't be distinguished. Therefore, the sum of their energies is registered, resulting in a summation peak in the spectrum. For example, the 583.2 keV and the 2614.5 keV gamma ray lines of ^{208}Tl are emitted ∼simultaneously (After emitting the 583.2 keV gamma ray, the resulting energy state, which emits the 2614.5 keV gamma ray, has a lifetime of 32 ps [20]). The result is a summation peak at 3197.7 keV. This and other summation peaks are present in the associated simulations as well as in measured data. The counts registered there will consequently be missing at the single energy peaks, which have then a lower detection efficiency.
For case two (Fig. 10) the efficiencies are two orders of magnitude smaller (if not scaled to the mass of the copper block as in the shown figure), which is due to the self-absorption of the copper. As before the shape for the different detectors agree, but this time they differ in the low energy range. Also, the efficiencies stay flatter with a

light decrease towards higher energies. While GeMSE, GeMPI II and GIOVE have a similar flat curve, Corrado and especially Bruno have a stronger decrease towards higher energies (∼60% for Bruno and ∼35% for Corrado). Moreover, the order of the detectors by the highest magnitude stays the same. The reason, why Bruno has a worse efficiencies compared to the others, is its sample chamber configuration. While for the other detectors the sample can be placed around the crystal, the sample in Bruno can only be placed in front of it. Also the sample chamber of Bruno is smaller. Therefore, a few kilograms of copper fill the chamber completely. This shows that the geometry of the sample chamber and hence how much copper can be placed inside it is predominant for this case.

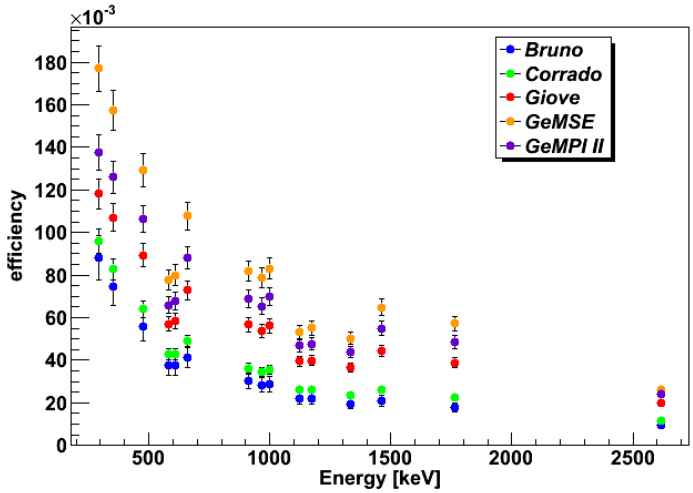

Figure 9: Efficiency comparison for the investigated detectors for the case using a point source

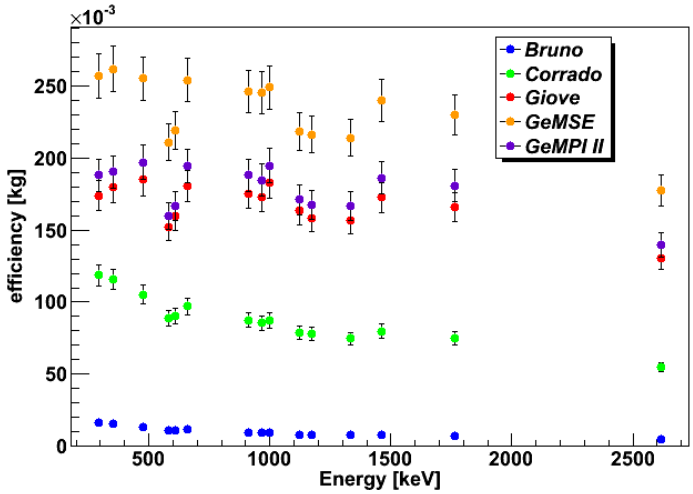

Figure 10: Efficiency comparison for the investigated detectors for the case using a full sample chamber, scaled to the mass of the copper block

In Tab. 2 the results of the achieved sensitivities are shown. The threshold activities for the detectors in the low-level laboratory are about an order of magnitude higher than the others, implying that they are less sensitive. The reason for this is the difference in meter water equivalent of the overburden.
One can also recognize the improvement from Bruno through Corrado to GIOVE. Bruno & Corrado are first generation HPGe detectors, while GIOVE (2nd gen) and its shield were optimized for the operation at shallow depth. In general, the sensitivity of GEMPI II is by a factor of about 1.5 better compared to GeMSE. But one has to note, that the laboratory where GeMSE is operated has a ∼5.5 lower water equivalent rock layer overburden.
It is noticeable that GEMPI II has an increased value for ^{137}Cs. This needs further investigation. Moreover, GeMSE has an increased ^{60}Co value, which might be explained by the low age of the detector. The inner shielding also consists of copper, which was most likely cosmogenically activated during production, transportation, and storage at the Earth's surface. This might have resulted in the production of radioactive isotopes with long half-lives such as ^{60}Co ($T_{1/2} = 5.26\,\mathrm{y}$), which still can be present in the material and have a possible impact on the background [21].

4 Conclusion

The procedure described in this study introduced defined standards e.g. normalization to a certain measurement time and the use of reference samples, representing the two extreme cases of sample configurations in gamma spectroscopy. Therefore it can be applied to other detector setups to obtain a comparable value for the sensitivity of the detector.
This study showed that GeMPI II is the leading germanium spectrometer with the highest sensitivity. The achieved sensitivity level is $\leq 30\,\mu\mathrm{Bqkg}^{-1}$ for primordial radionuclides from U and Th. A sophisticated veto system ensures a high virtual depth and consequently a high background suppression. Yet, GeMPI II and GeMSE operate in the same sensitivity range, closely followed by GIOVE.

	sample chamber configuration									
	class 1: small low-mass samples represented by point-source					class 2: large high-density samples represented by copper block				
	threshold activity [mBq]					threshold activity [mBq/kg]				
Isotope	Bruno	Corrado	GIOVE	GEMPI II	GeMSE	Bruno	Corrado	GIOVE	GEMPI II	GeMSE
^{238}U	56.08	39.95	12.01	1.86	3.64	168.57	16.26	3.23	0.67	1.22
^{226}Ra	1.06	0.70	0.19	0.042	0.069	3.75	0.36	0.071	0.019	0.030
^{228}Th	1.69	1.15	0.33	0.081	0.12	3.99	0.37	0.046	0.020	0.031
^{228}Ra	1.74	1.19	0.35	0.084	0.11	5.32	0.49	0.11	0.030	0.037
^{137}Cs	0.59	0.44	0.12	0.027	0.026	2.16	0.22	0.034	0.012	0.011
^{60}Co	0.40	0.28	0.13	0.023	0.066	1.03	0.09	0.025	0.006	0.016
^{40}K	11.60	4.07	1.68	0.35	0.47	29.96	1.34	0.22	0.10	0.13

Table 2: Achievable sensitivity with the evaluated HPGe-Detectors for 30 days counting time. For two classes of samples the threshold activity for various radioactive isotopes is calculated.

Part III
Characterization of a Coaxial Well Gamma Spectrometer

1 Motivation

The Max-Planck Institut für Kernphysik (MPIK) in Heidelberg is involved in the research of Dark Matter (XENON1T) and other low background experiments. For radiopurity investigations of materials used in these experiments, the MPIK operates three high purity germanium spectrometers in the Low-Level Laboratory (LLL). The LLL is located under soil and concrete overburden, corresponding approximately to 15 m of water equivalent. The existing three gamma spectrometers (Bruno, Corrado, GIOVE) in the LLL are coaxial p-type detectors. Consequently, the measured samples are not surrounded by the sensitive crystal and can only be placed in front of the crystal instead. This results in a lower detection efficiency than a 4π surrounding detector.
The configuration of coaxial p-type detectors is also disadvantageous especially for low energy gamma rays e.g. the 46.5 keV [1] gamma of ^{210}Pb. The detectors are not sensitive in this energy range since the low energy gamma rays are not able to penetrate the dead layer and therefore don't reach the active volume of the crystal. To solve these issues the coaxial well gamma spectrometer Adam is put into operation again. The detector was first installed in 1996 but was shut down at some point due to an insufficient and broken muon veto. Its setup including the lead shield was removed a few years later. Now the detector and a new shielding system are going to be reinstalled. This part of the thesis is about the characterization of the Adam detector and its implementation in a software model used for data analysis.

2 General description of the detector & Commissioning

2.1 Coaxial well type & Crystal parameters

The Adam detector is a coaxial well p-type detector made out of high purity germanium (HPGe). On the outer surface a thin layer of lithium is diffused into the germanium, called the n-doped layer of the diode (see Sec. I.2.3). The p-contact is made by application of boron in the borehole. As mentioned in Sec. I.2.3 these areas are not sensitive for gamma radiation and form the so called dead layer.
The crystal is turned by 180° compared to a standard coaxial detector. Thus, the borehole points into the front direction and the sample is placed directly into it (see Fig. 12(a)). This has the consequence that only samples which fit into the hole can

[1] If not otherwise stated, all gamma energies in the following are taken from [21].

be measured. Nonetheless, the advantage of having a nearly 4π crystal surrounded sample is significant and improves evidently the detection efficiency. Additionally, by having the sample in the borehole there is no thick dead layer since the doping of the boron is only a few hundred nanometers deep. In comparison, the dead layer of the lithium is usually around 0.7 mm [3]. Moreover, the end cap inside the borehole is produced as thin as possible. Hence, low energy gamma rays should be able to penetrate the end cap material and the dead layer to deposit their energy in the sensitive part of the crystal. This enables the MPIK to perform low energy gamma ray spectroscopy, which was not possible with the available gamma spectrometers at the LLL.
When this work was started little information about the setup was available. Essentially, only the crystal dimensions were shown in a sketch. Later a more detailed drawing was found, which however was not used in this work. For comparison, it is attached in Fig. A.1. According to the dimensions from the sketch the crystal has a volume of 90 ccm. The general composition of such a detector is that the crystal is placed in a holding cup which is vacuum insulated by the end cap (see Fig. 11).

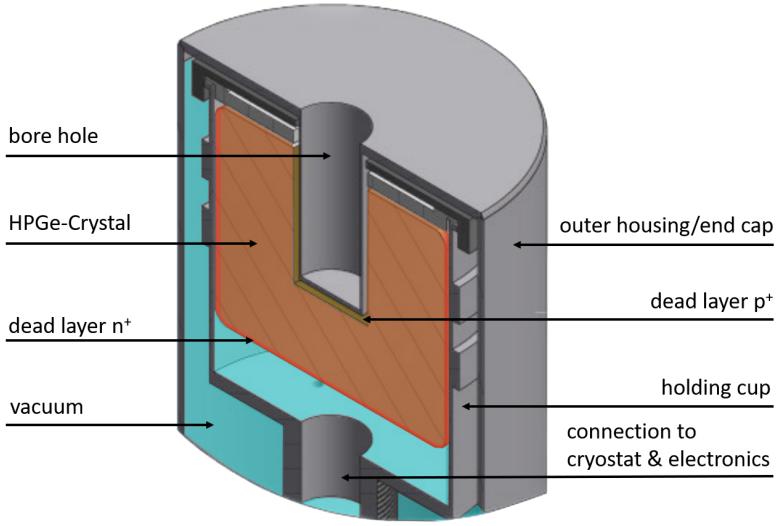

Figure 11: General structure of a HPGe well detector [22]

2.2 Internal structure & End cap

Besides the sketch of the crystal dimensions, there was no knowledge about the detector itself, the crystal position, the mounting of the crystal or the used materials. There was also no insight of the electronics or the connection of the cooling finger. The dimensions of the end cap including the borehole were measured with a caliper. Since the material is unknown, it was assumed that the end cap is made out of monel (64% Ni, 31% Cu, Mn, Fe, Si). This assumption was based on the knowledge that the end cap of another detector of the same manufacturer, which is not in operation anymore, was made out of monel as well.

2.3 DAQ & Detector operation

For data acquisition, the signal of the detectors preamplifier is transferred via a main amplifier to a MCA connected to a computer. A reversed bias high voltage is required for the detector operation (Sec. I.2.3). The high voltage (HV) setting should be adapted to get a high count rate and a good energy resolution. An old data sheet suggested a HV of 1200 V. To make sure the diode is in the plateau of the reverse bias and thus small fluctuations in the HV do not influence the count rate significantly [3], the count rate was measured for multiple high voltage settings. No increase or decrease of the count rate could be observed and the HV was fixed at 1200 V. In a next step, the signal rise time, as well as the pole-zero cancellation of the amplifier were adjusted to get a good signal. This was done by looking at the signal from the amplifier on an oscilloscope and adjusting the parameters accordingly.

3 Implementation & Optimization of the software model

3.1 Basic implementation

To operate a germanium spectrometer for low-level gamma spectroscopy a Monte Carlo simulation of the detector is needed to analyze the sample activities (see eq. 1). The simulation accounts for different sample geometries and determines the detection efficiency for each configuration accordingly. The geometry of the Adam detector was coded in the *Geant-4* based simulation software *MaGe* [23]. In *MaGe* many different geometric shapes can be simulated, which will be used to compose the detector in a building block manner. The individual parts get their materials assigned and the behavior of the gamma radiation passing through them is simulated by the program. The simulated germanium crystal excluding the dead layer then equals the active volume of the detector. Energy depositions in this volume by different simulated processes e.g. photo effect, Compton scattering or bremsstrahlung of produced electrons, are registered by the program and saved in a *Root*-file.
Due to the lack of information about the detector some simplifications had to be made. In the simulation, the electronics, the mounting of the crystal and the connection to the cryostat were not implemented. Furthermore, it was assumed that the crystal sits in a vespel cap (polymer: 93.3% N, 6.7% H) with a thickness of 0.6 mm. This is justified since this is a usual material and thickness for the crystal mounting. The thickness of the assumed monel as the end cap material was estimated to be 2 mm. Another unknown factor in the composition of the detector is the position of the diode inside the end cap. It was tried to measure the position with a collimated ^{241}Am source, but the available source strength (5 MBq) turned out to be too weak. This is most likely due to two reasons. First, the thickness of the monel on the outside prevents most of the gamma rays of the americium to reach the crystal. The second issue is the background radiation, making the desired gamma lines unobservable. It seems logical to assume that the crystal is as close to the front window as possible. This was done while keeping the vacuum layer around

the borehole homogeneous. Thus, the vacuum at the back of the borehole is as thick as the vacuum around it. The final software model can be seen in Fig. 12 (b).

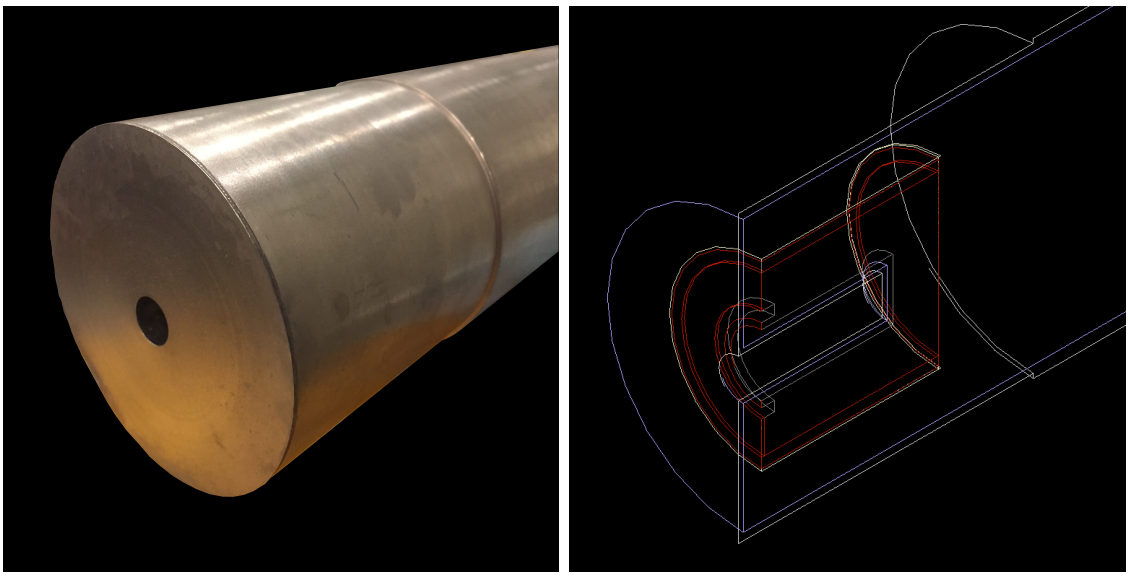

(a) Adam detector (b) Basic Monte Carlo model

Figure 12: Comparison of the real detector and the Monte Carlo Model

Since a lot of assumptions had to be made in the Monte Carlo implementation, the general strategy for the optimization was the following: The thickness of the dead layer on the crystal mantle and of the monel inside the borehole as well as the monel at the front have to compensate for the lack of knowledge (see Fig. 13). This was done by adjusting their thicknesses to match the simulation to the real data, which is described in the proceeding sections. For this task, the thicknesses of the dead layer and the monel were defined as variable parameters for individual areas around the detector (e.g. borehole side & borehole back, etc.). Each thickness can then be inferred by matching a measurement to the simulation of different thickness. The reason for the distinction between monel thickness and dead layer thickness is described subsequently: The dopance of the front side (see Fig. 13) of the crystal is not clear, since it could not be doped at all but could also have different dopants. Consequently, the thickness of the monel is chosen to be the defining quantity. The borehole itself is doped with boron to make the p^+-contact of the diode. The arising dead layer of this dopance is usually about 300 nm thick [3]. Therefore, gamma rays passing it are barely influenced ($\sim 3.25 \cdot 10^{-5}\%$ Attenuation for a 100 keV gamma ray [5]). Again the thickness of the monel is the important quantity here.
It is vital to note that effective thicknesses are going to be determined. These cannot be seen as equivalent to the actual dead layer of the crystal and the thickness of the end cap. They are designed to include the assumptions (e.g. thickness of the monel on the mantle) mentioned above to match the simulation to the real world situation. By doing this, any influence of the neglected parts or assumed properties

discussed earlier should be considered in the simulation, which consequently should yield comparable results to the real situation.

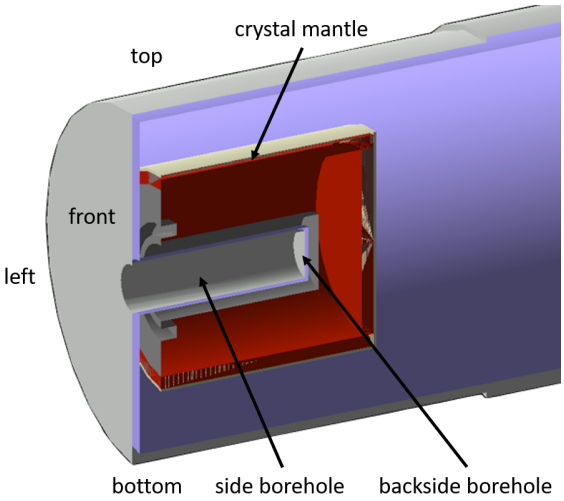

Figure 13: Illustration of the positions of the different measurements. The dead layer thickness is determined on the mantle at four different positions (see Sec. III.3.2). The monel thickness determination inside the borehole and at the front is done in Sec. III.3.3.

3.2 Determination of the dead layer thickness

3.2.1 Experimental procedure

The dead layer itself represents a plane that has to be passed by gamma radiation before reaching the active volume in the crystal. Consequently, the thicker the dead layer the lower the count rate of the low energetic gamma rays (see Fig. 14). The thickness of the dead layer can be inferred by matching the measured count rate of a monoenergetic gamma line to the simulation of varying dead layer thickness.
Thereby, certain assumptions were made. The doped surface of the diode is entirely covered by a homogeneous dead layer of constant thickness with a charge collection efficiency of 0. Events depositing partly their energy in this layer do not contribute to the full energy peaks. Local variations of the dead layer along one specific surface are not accounted for. Apart from the dead layer, a charge collection efficiency of 1 is assumed. The remaining volume of the crystal (excluding the dead layer) is then referred to as the active volume (AV). Consequently, regions with reduced charge collection even at nominal voltage, e.g. in corners, do not exist. A more detailed determination including a differentiated area analysis was not done. This would have required a collimated source, which was not available as mentioned before. In the following the measurement procedure is described in more detail.
The dead layer measurement was carried out with an uncollimated ^{241}Am source having an activity of 370 kBq. By using an uncollimated source one obtains an aver-

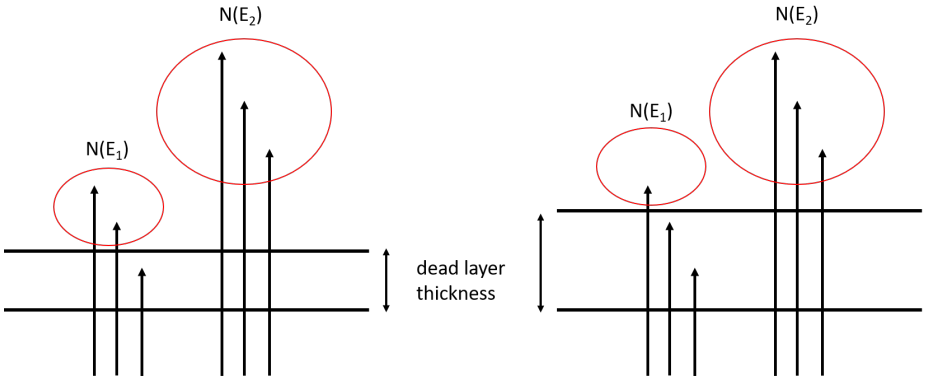

Figure 14: Illustration of the influence of the dead layer thickness on the count rate N of low energetic gamma rays E_1 and high energetic gamma rays E_2.

age value of the count rate over the illuminated part of the detector. The dominant gamma energies of americium are 59.53 keV, 98.97 keV and 102.92 keV with branching ratios of 35.92%, 0.0203% and 0.0195%, respectively.
In principle, one could use just one low energy gamma peak and calculate the absolute detection efficiency (ADE) for this line, given by the ratio of the count rate in the full energy peak (FEP) and the count rate of the isotropic emitted photons by the source. By comparing the experimental value with the one of the simulation for varying thickness of the dead layer, the thickness can be extrapolated. One finds

$$ADE = \frac{N_{FEP}}{N_{emitted}} = \frac{N_{meas.}}{A_\gamma \cdot t_{meas.} \cdot \beta} \quad , \tag{12}$$

where β is the branching ratio of the line under investigation and A_γ the activity of the source, calculated by

$$A_\gamma(t) = A_0 e^{-\lambda t} \quad , \quad \lambda = \frac{\ln 2}{T_{1/2}} \quad , \tag{13}$$

where A_0 is the total activity of the calibrated source given by the manufacturer and $T_{1/2}$ the half-life period ($T_{1/2} = 432.6$ a for ^{241}Am [3]) .
This procedure has the disadvantage that it is dependent on the source activity, which was not known precisely enough. Also, the positioning of the source, as well as the dead time of the detector (especially if the source is near to the detector), can lead to significant deviations.
To avoid this, one uses multiple gamma lines of the same source instead. Then the ratio of the counts of the low energetic gamma rays ϵ_{lowE} and the counts of the high energetic ones ϵ_{highE} is taken for the analysis (see eq. 14). As a result, the activity of the source and the mentioned effects cancel out.
In the specific case of the ^{241}Am source, the three dominant gamma lines mentioned above are perfectly suitable. The energies of the emitted photons are in the low energy range, in which the dead layer thickness is most relevant. Consequently, the

intensity of the low energetic 60 keV-line is significantly stronger influenced by the dead layer than the high energetic lines of 99 keV and 103 keV. In addition, due to their short range in germanium ($\frac{1}{e}$ attenuation after ~ 3.4 mm [5]), these low-energy gamma rays are not affected by the dimensions of the crystal borehole.
Since the two high energetic lines lie close together and each has a rather low branching ratio, their sum was taken to form the ratio

$$r = \frac{\epsilon_{lowE}}{\epsilon_{highE}} = \frac{\epsilon_{60}}{\epsilon_{99} + \epsilon_{103}} \quad . \tag{14}$$

In the actual measurement the source was placed at varying distances (0 cm, 1 cm and 5 cm) above the detector and the energy spectrum was measured for each case. The measurements for different distances were done to probe whether the angular distribution of the source or the dead time of the detector have any influence. The experimental set-up for a source-detector distance of 5 cm is shown in Fig. 15. A provisional lead shield was built to reduce the surrounding background. Due to the low emission probability of the two high energy lines a several hours long measurement was required to get sufficient statistics ($>10^5$ net counts in each peak).
To test the assumed homogeneity of the dead layer thickness around the crystal several control measurements were done. Altogether measurements from all detector sides (right and left at a distance of 5 cm as well at the bottom with distances of 0 cm and 5 cm, see Fig. 13) have been performed. To form the ratio for each of the measurements one needs to extract the count rate of the three investigated gamma lines from the measured energy spectra. This is done in the proceeding section.

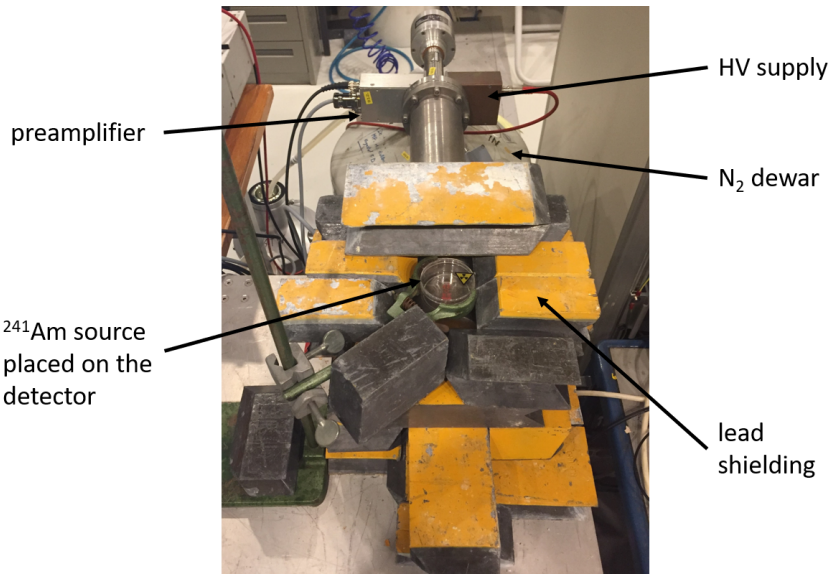

Figure 15: Experimental set-up for the dead layer thickness determination. The source inside a plastic box was placed on top of the detector to determine the dead layer on the outer mantle.

3.2.2 Data analysis

Since two of the investigated peaks have energies close to each other, they most likely overlap and the application of the standard definition for the region of interest (DIN norm 25482-5 for gamma spectroscopic investigations) was not possible. A Gaussian fit of the peaks was not suitable due to some tailing towards low energies. These tails arise due to the not complete charge collection efficiency (CCE) outside of the dead layer as assumed in the simulation. In contrary, the doped layer consists of an inactive dead layer (CCE=0) and a semi-active transition layer in which the charge collection efficiency is <1. The total thickness of these two layers is called full charge collection depth (FCCD). Events depositing their energy in the transition layer still produce electrons proportional to the energy, but only a part of these electrons are collected. The reduced charge is still measured but will not contribute to the full energy peak and rather produce the low energy tail next to the FEP.
A *crystal-ball* function [24] was used to take these tails into account. Additionally, a background function was fitted to include the continuous background. The fit results are given in Fig. 16. For the energy of 99 keV & 103 keV two overlaying *crystal-ball* functions have been fitted.

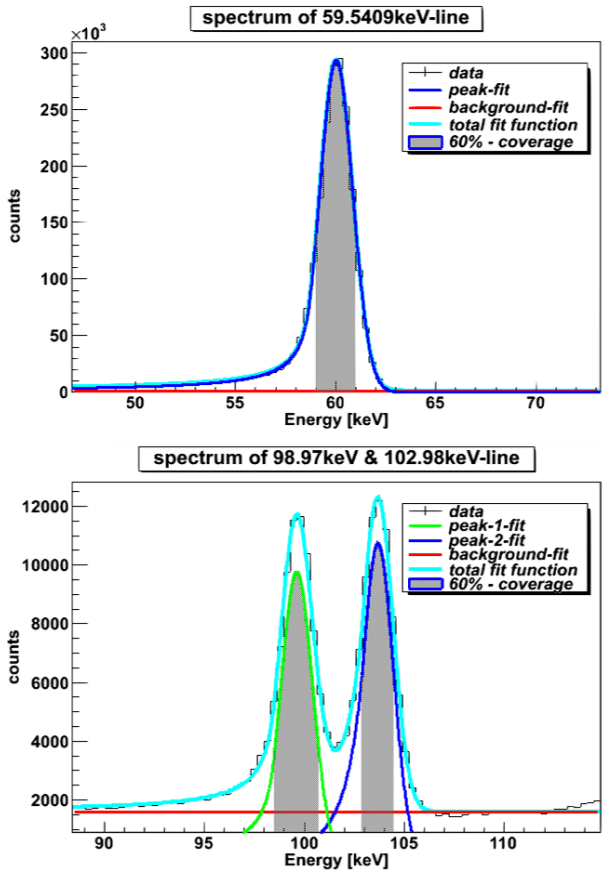

Figure 16: Measured gamma energies of 241-Am with resulting and individual fit functions. The shaded areas represent the 60%-coverage area.

To not include all the counts in the tails, a 60%-coverage area around the mean of the fit function was defined, which equals 60% of the integral count rate of the fit function. This is a valid approach since in the calculation only the ratio is of importance. The defined 60%-coverage areas are also shown in Fig. 16. The desired ratio was then calculated using eq.14 with the integral count rate of the 60%-coverage area of each individual peak.
To obtain the value for the ratio a constant background was used in the previous fit. Actually one would expect a decreasing background towards higher energies, but a constant background fit was used since the energy range of the fit was small enough. As a systematic check, the fits were redone allowing for a linear decreasing background. The error of the ratio was then estimated to be the deviation of the ratios between the fit with the two background functions. The error of the fit parameters were subdominant to this estimate and were neglected.

3.2.3 Simulation

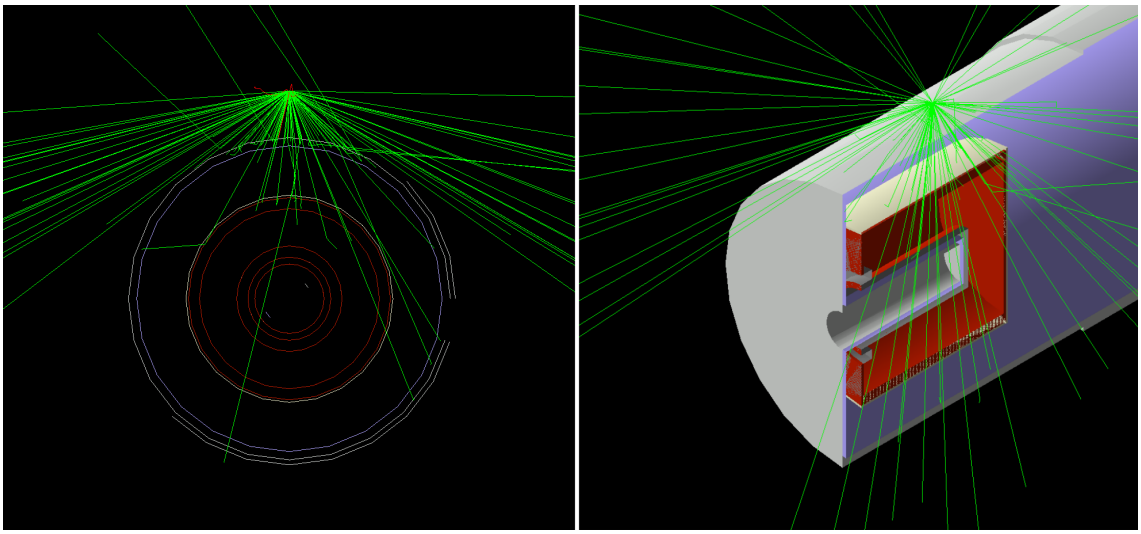

Figure 17: Illustration of one of the simulations with a few generated events.

For the matching with the data the ratio of the same three gamma lines and varying dead layer thickness had to be simulated with the software model of the detector. For this task, each of the three gamma rays with fixed energies was simulated individually by starting 30 Mio. gammas from a point source at a position with the same configuration as the experimental set-up before. One of the resulting simulations is shown in Fig. 17 displaying a few simulated events.
The detection efficiency ϵ_i is given by the quotient of the detected gammas and the emitted ones. By taking the branching ratios β_i of the three gamma lines, the ratio is obtained by

$$r_{sim} = \frac{\epsilon_{60} \cdot \beta_{60}}{\epsilon_{99} \cdot \beta_{99} + \epsilon_{103} \cdot \beta_{103}} \quad . \tag{15}$$

The error of the calculated ratio r_{sim} was computed with Gaussian error propagation using the square-root error of counting statistics. Since this resulted in an error in the order of 0.01%, which was due to the high number of started events, an error of 3% was estimated to account for the observed smearing of the peaks in the data.
The described simulations were repeated for different distances of the point source to the detector (the same as described in Sec. III.3.2.1) and more important for varying dead layer thicknesses. In particular for each distance the dead layer was varied from 2 mm to 4 mm in 0.1 mm steps. For each step, the above described simulations were carried out and the respective ratio of the gamma lines was computed.

3.2.4 Results

The simulated ratio of the gamma lines had to be matched to the experimentally acquired ratio. In Fig. 18 the simulated ratios for varying thickness of the dead layer are plotted versus the dead layer thicknesses for the case where the source was placed at a distance of 5 cm above the detector. The data points were fitted according to the Beer-Lambert law [3].
The dead layer thickness for each measurement was obtained by comparing the measured ratio with the fit function. Similarly, the errors were obtained by using the maximal or minimal value of the measured ratio in its error range respectively. The error bands are also shown in Fig. 18 by the dashed areas. The error of the experimentally obtained ratio is dominant and the error of the exponential fit could be neglected. The resulting dead layer thicknesses for all measurements are shown in Tab. 3. For the positions see Fig. 13.

position	top	bottom	left	right
distance	dead layer thickness [mm]			
5 cm	2.42±0.18	2.82±0.17	2.81±0.15	2.73±0.22
1 cm	2.67±0.17	-	-	-
0 cm	2.44±0.12	2.93±0.19	-	-

Table 3: Overview of the determined dead layer thickness

It was found that the dead layer at the top of the detector seems to be significantly smaller than everywhere else. The determined values for the dead layer thickness for the other three sides agree well within their errors.
For a complete description of the dead layer, a continuous scan employing a collimated source would have been needed. As mentioned in Sec. III.3.2.1 a dedicated facility and source were not available. Because of that, the homogeneity assumption was kept and an overall average of the dead layer thickness of the mantle was

calculated. This is legitimate since it will not have any impact for the low energy measurements of samples inside the borehole.
To avoid overcounting the top in the average only the measurements for a distance of 5 cm were averaged (weighted). This yielded (2.71 ± 0.09) mm as the final value for the thickness of the effective "dead layer" on the mantle. This value is also taken for the thickness at the backside, since the dead layer there can't be measured.

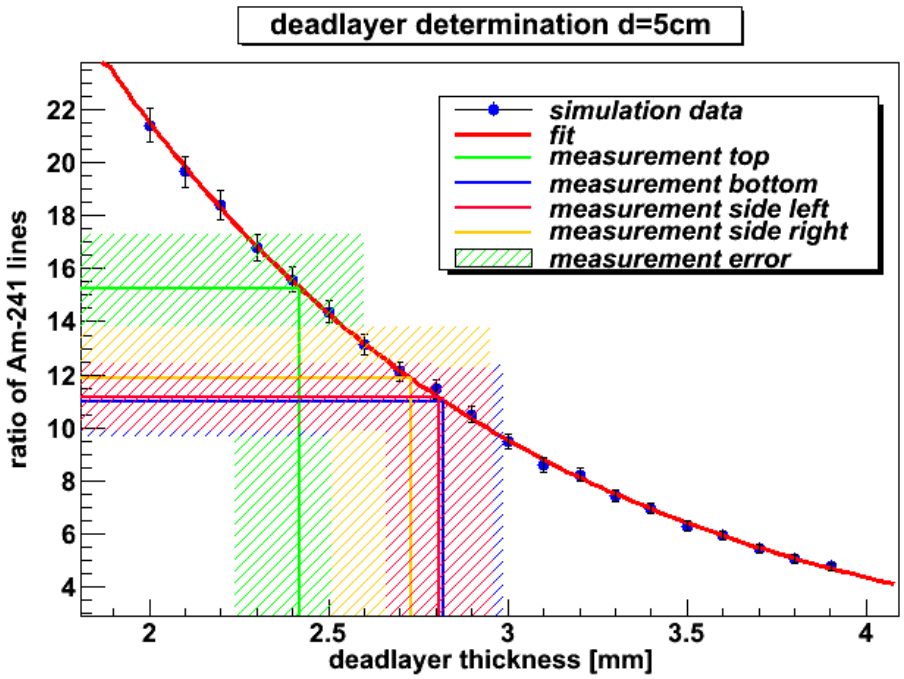

Figure 18: Fit of the Beer-Lambert law to the simulated data. The colored lines represent the different positions. The dashed areas show the measurement errors.

3.3 Estimation of the end cap thickness inside the borehole & the front

So far the dead layer of the mantle has been determined. The next step was to characterize the front and the borehole. This was the most crucial parameter since in the end, the sample is going to be placed inside the borehole. As explained in Sec. III.3.1 the monel thickness is the substantial quantity to be determined.
First, the monel thickness at the front was determined. This time a collimated ^{241}Am source with an activity of 5 MBq was used. For this measurement, the activity was sufficient since the end cap thickness is thinner than the one at the side. The source was pointed directly at the end cap, next to the borehole (not pointing into the borehole) and measurements for two different distances (0 cm & 5 cm) were made. The measurement procedure was generally the same as the one described in the previous section, but this time the varying end cap thickness and not the dead layer

thickness was simulated. The determination and the error estimation was done as before. The obtained values are shown in Tab. 4.
The monel thickness determination inside the borehole was split into two parts. The thickness at the backside and the thickness at the sides (see Fig. 13) were specified individually. For the first part, the collimated source was placed in front of the end cap and pointed directly into the borehole. Similar to before the thickness of the monel was obtained by comparing the experimentally gained ratio of the ^{241}Am with the simulated ratio's (see Fig. 20). The result is shown in Tab. 4.
Since the collimated source couldn't be pointed to the side of the borehole, the determination of the monel thickness at the side of the borehole required a source which only emits gamma rays to the side and not to the back of the borehole. This was made possible with the set-up shown in Fig. 19.

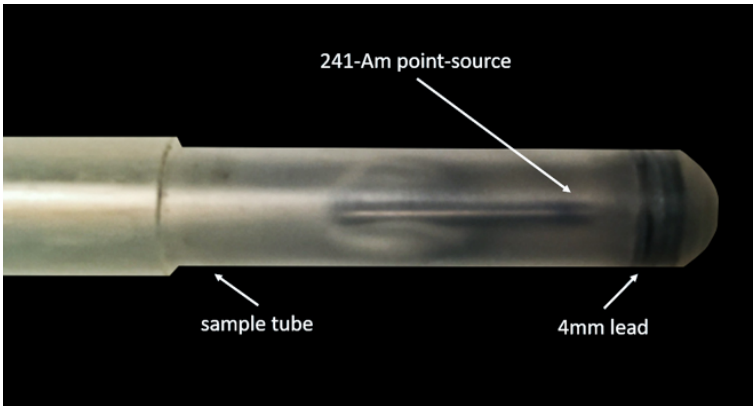

Figure 19: Sample tube with 241-Am source and lead shield in front to avoid radiation into this direction.

Four 1 mm thick lead plates were placed at the bottom of a sample tube to shield the emitted radiation directed to the backside of the borehole. The used tube is a standard plastic tube, which was abraded to fit perfectly into the borehole. Later such a tube will be used to place the samples into the detector. Behind the lead shielding a 3 kBq ^{241}Am point source was placed and fixed with vacuum paste. With this structure, only the gamma rays emitted to the side should be able to reach the crystal. The distance in lead, where the intensity of a 100 keV gamma is attenuated by 50%, is 0.014 cm [25]. The resulting attenuation is in the order of 10^9. Therefore the gamma rays directed to the backside should be shielded completely by the lead. The sample tube was placed inside the borehole and the energy spectrum was measured for two different configurations. The source was placed at 1.4 cm and 2.9 cm relative to the entry of the borehole. This was done to test the homogeneity along the length of the borehole. The same two configurations were simulated including the sample tube and the lead shield. The extrapolation of the obtained ratios is shown in Fig. 20. The resulting values of the monel thickness are given in Tab. 4. For the positions see Fig. 13.

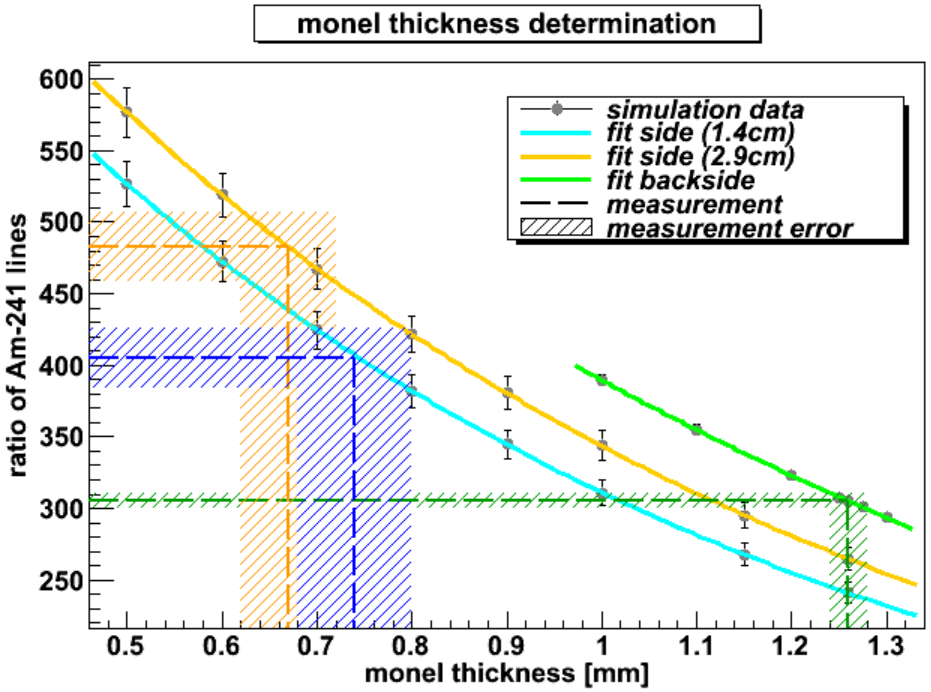

Figure 20: Fit of Beer-Lambert law to the simulated data to obtain the monel thickness inside the borehole. The dashed, colored lines represent the different measurements. The dashed areas show the measurement errors.

	outside-front	side borehole	backside borehole
monel thickness[mm]	(0 cm) 1.77±0.07	(1.4 cm) 0.74±0.06	1.26±0.02
	(5 cm) 1.63±0.02	(2.9 cm) 0.67±0.05	
average	1.64±0.02	0.70±0.04	1.26±0.02

Table 4: Overview of the determined monel thicknesses

For the monel thickness at the outside-front a slight deviation is observed. This might be explained due to the angular distribution for the different distances. Additionally, the measurement with greater distance could have been influenced by gamma rays directed into the borehole. It is also possible, that different dopants play a role. Still, the values agree in the error range and the average is taken as the final value.

The obtained values of the monel thickness for the sides of the borehole and the backside of the borehole do not agree with each other. Consequently, the thickness inside the borehole could not be assumed to be completely homogeneous. Thus, they were implemented separately in the software model. This is in agreement with modern well detectors, whose backside of the borehole is thicker than the sides [22]. The two obtained values for the side agree within their errors and the thickness on the sides is assumed to be homogeneous. Their weighted average is taken as the final value for the monel thickness for the mantle inside the borehole, which is also shown in Tab. 4.

3.4 Active volume adjustment

The measurement of the dead layer thickness on the mantle of the crystal was done from outside and the thickness of the dead layer was adjusted accordingly. Since the dead layer thickness is dependent on the assumption of the monel thickness, but the active volume is not, the AV could have been wrongly estimated by this approach. Thus, the active volume had to be adjusted to the previously determined quantities. For this task, a ^{60}Co source with an activity of (1763 ± 34) Bq was used. ^{60}Co has high energy gamma lines, which have a mean free path in germanium equal to the crystal size ($\sim$2 cm) [5]. The gamma rays can pass the entire crystal and their count rate is therefore a direct measure for the size of the crystal's active volume.
The ^{60}Co source was placed directly on top of the detector and the energy spectrum was measured for 7520 s. Using eq. 12 a comparison of the absolute detection efficiency of the 1332.5 keV line with simulations for varying active volumes (radius of the crystal was adjusted) was done. The result of this measurement was the reduction of the crystal radius from 2.435 cm (from the technical drawing) to (2.34 ± 0.01) cm. The active volume of the model is consequently smaller than suggested by the sketch of the crystal dimensions. This is most likely due to a small underestimation of the monel thickness on the outer mantle. By considering the reduced active volume in the software model this error has no impact on the subsequent simulations.
With the previous optimizations, the germanium crystal in the software model has an active volume of 52.5 ccm and an active mass of 0.280 kg.

4 Estimation of the influence of different background components

4.1 Background measurement

Once the optimization of the software model was completed, it was used to investigate the detectors background spectrum. First, the background spectrum without any shielding was measured for several days.

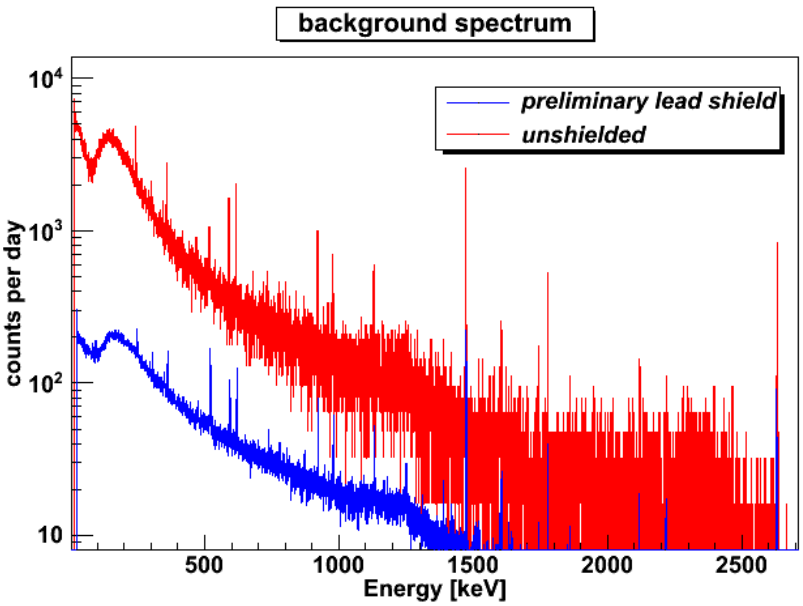

Figure 21: Comparison of the background spectrum with & without lead shield. The provisional lead shield leads to a significant background reduction. The shielded spectrum is shown in Fig. 22 for the full energy range, while Fig. 23 shows the low energy range.

The spectrum (counts per day) is shown in Fig. 21 for the energy range 30 keV to 2700 keV. Below 30 keV the count rate rises steeply most likely due to microphonic noise. Another background measurement was performed after installation of a preliminary lead shield, which was similar to the one used for the dead layer measurement, but this time the 'entire detector' was shielded. The obtained spectrum is shown in comparison to the unshielded spectrum in Fig. 21. The provisional lead shield reduces the overall background count rate by a factor of 22. The background spectrum with a provisional lead shield is also shown in Fig. 22 in the full energy range, while Fig. 23 shows a zoom in the low energy range. In the following, the spectral shape and the origin of the observed peaks are discussed in detail.

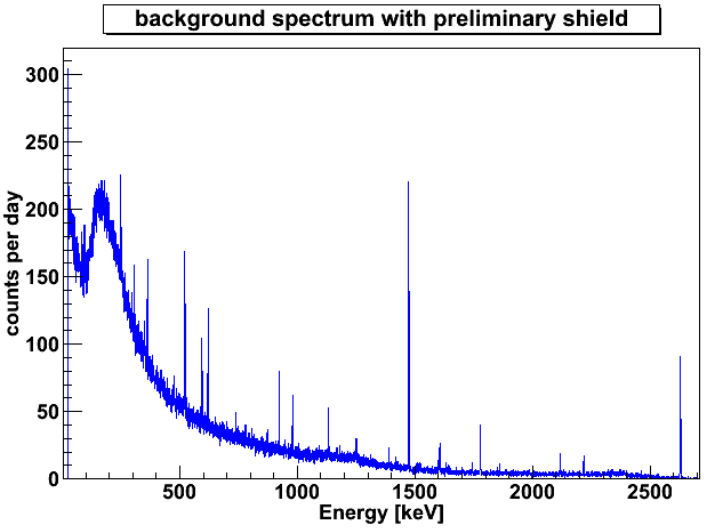

Figure 22: Background spectrum with a preliminary lead shield, scaled to counts per day.

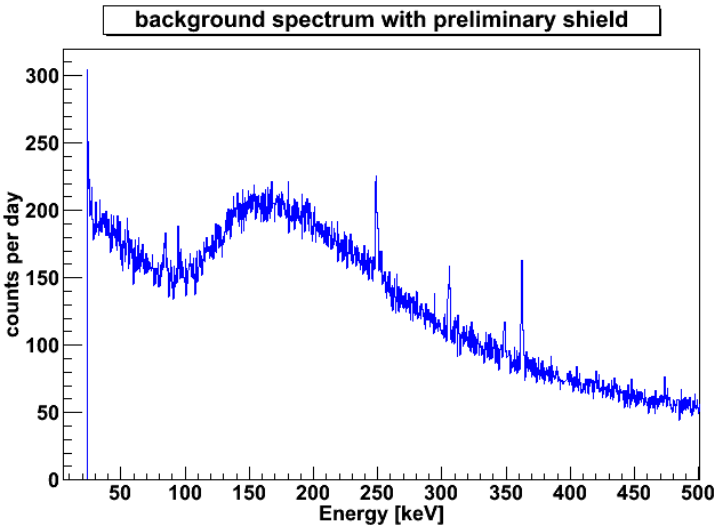

Figure 23: Background spectrum with shielding in the low energy range

4.2 Background of the environment

Natural radioactivity in the environment (see section I.3) is the dominating background source if there is no proper shielding. The major gamma lines in Fig. 22 are identified in Tab. 5. Besides the full energy peaks, these isotopes also contribute to the count rate of the spectral ridge and the overall background e.g. via bremsstrahlung (see section I.3). The ridge or the valley, respectively, arise due to the efficiency drop towards lower energies. Most of the lower energy gamma rays from the outside are attenuated by the detector materials resulting in a lower detec-

tion efficiency. This efficiency drop competes with the attenuation coefficient of the germanium shown in Fig. 2, resulting in the typical background spectrum. The rise in the lowest energies is due to microphonic noise and due to neutron interactions, which will be discussed later.

Subchain	Isotope	Energy [keV]	Subchain	Isotope	Energy [keV]
^{226}Ra	^{214}Pb	295.22	^{228}Ra	^{228}Ac	968.96
	^{214}Pb	351.92		^{228}Ac	911.20
	^{214}Bi	609.31	^{228}Th	^{212}Pb	238.63
	^{214}Bi	1120.29		^{208}Tl	583.2
	^{214}Bi	1764.49		^{208}Tl	2614.53
-	e^+e^-	511	^{40}K	^{40}K	1460.8

Table 5: Identified energies shown in the background spectrum (Fig. 22).

From Tab. 5 one can conclude that ^{228}Th & ^{226}Ra (present in the concrete) contribute significantly to the background. For the purpose of low energy gamma spectroscopy the peaks below 100 keV are of particular interest. The two peaks at low energies, ∼76 keV & ∼86 keV, are caused by the preliminary lead shielding used during the measurement. According to [13] those arise from X-ray radiation of the lead, induced by the ^{210}Bi decay, but also via excitation by muon-induced electrons in the lead. The background arising from muons and the lead-induced background are discussed in the following.

4.3 Muon induced background

Even in well-shielded detectors muons, originating from the cosmic radiation, are an unavoidable source of background events. Muons are produced by the interaction of the cosmic ray background with the earth's atmosphere (see Sec. I.3.3). At the depth of the LLL, the cosmic ray muon flux is reduced only by a factor of ∼2 to 3 [13]. Therefore, a high muon veto efficiency is required for the background reduction. The muons reaching the detector contribute to the background e.g. by ionization of the diode or by secondary reactions with the shielding material. For muons with an energy less than ∼10 GeV muon capture in lead occurs, which produces neutrons [12].
In the depth of the LLL, the neutron flux of the primary hadronic component of the cosmic ray background is two orders of magnitude smaller than the neutrons produced by cosmic ray muons [26]. The produced neutrons interact with the germanium and can excite nuclear states.

The most probable interactions are inelastic scattering with fast neutrons and thermal neutron capture [27]. When these interactions take place in the germanium of the detector, characteristic gamma lines arise in the spectrum.
Inelastic neutron scatter typically appear as broad and asymmetric peaks with tails towards high energies (saw tooth shaped peaks) [12]. They arise because the recoil energy deposition and the energy of the gamma rays sum up. The most prominent ones are 596.4 keV (^{74}Ge(n,n')) and 691.4 keV (^{72}Ge(n,n')). The most intensive gamma lines produced by neutron capture are at 139.9 keV (^{74}Ge(n,γ)^{75m}Ge) and 198.4 keV (^{70}Ge(n,γ)^{71m}Ge) [27]. Both have standard Gaussian shapes. These gamma peaks can be used to characterize the neutron field present in the detector surrounding. The simulated spectra of these gamma energies are shown in Fig. 24 for the neutron scattering and in Fig. 25 for the neutron capture.

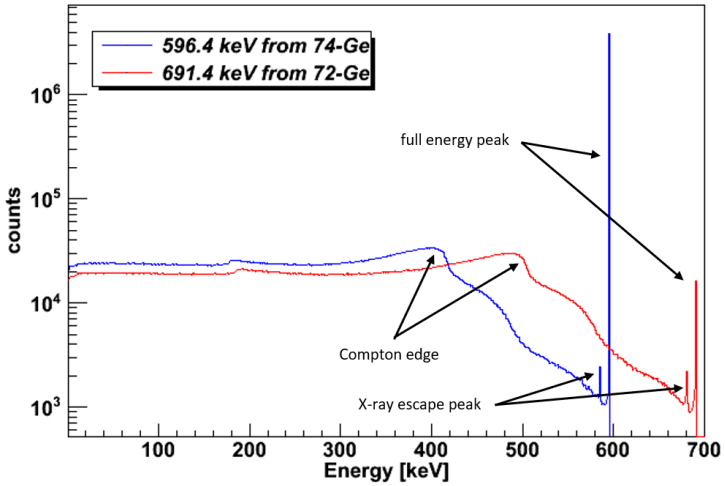

Figure 24: Simulated spectrum of the most probable gammas produced by neutron scattering in germanium. 30 Mio. events were started.

Thereby, the neutrons were not simulated directly but only the induced gamma energies distributed homogeneously in the detector crystal. This explains why the simulated spectra don't show the before mentioned saw tooth shaped peaks from neutron inelastic scattering, since only the resulting gamma line but not the entire scattering process including the recoil has been simulated. The spectra show typical characteristics of a gamma spectrum such as the photopeak, the Compton edge as well as a backscatter peak. The backscatter peak arises by Compton scattering of an escaping photon with the detector material back into the germanium crystal, resulting in a peak at an energy equal to the full absorption peak energy minus the energy of the Compton edge. The peaks below the full energy peak arise if an X-ray (E$\sim$10 keV) emitted by an excited germanium atom escapes detection [21]. Due to the high background of the environmental radiation these peaks cannot be seen in the background spectrum and further analysis is postponed until a proper shielding including a muon veto is set up. The simulated spectra can then be used to get an estimate of the background contribution of these interactions.

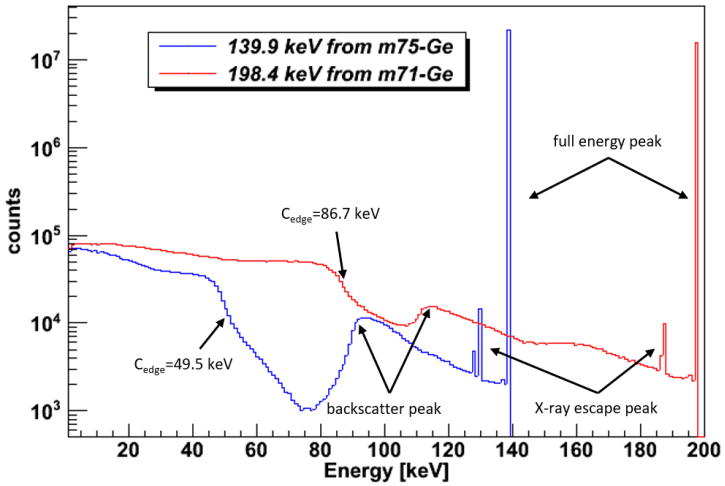

Figure 25: Simulated spectrum of the most probable gammas produced by neutron capture in germanium. 30 Mio. events were started.

Another contribution of neutrons to the background is elastic scattering (n,n). The involved nucleus recoils and the energy will be registered in the detector material. For elastic scattering this energy deposition will show up on the low end of the spectrum towards zero energy [12]. Depending on the energy of the incoming neutron, this distribution can go up to a few tens of keV. Additionally to the microphonic noise, this might explain the high count rate to low energies in the background spectrum (Fig. 22). Without a proper shield, this cannot be further distinguished from microphonic noise. A schematic spectrum showing the characteristics of these neutron interactions is shown in Fig. 26.

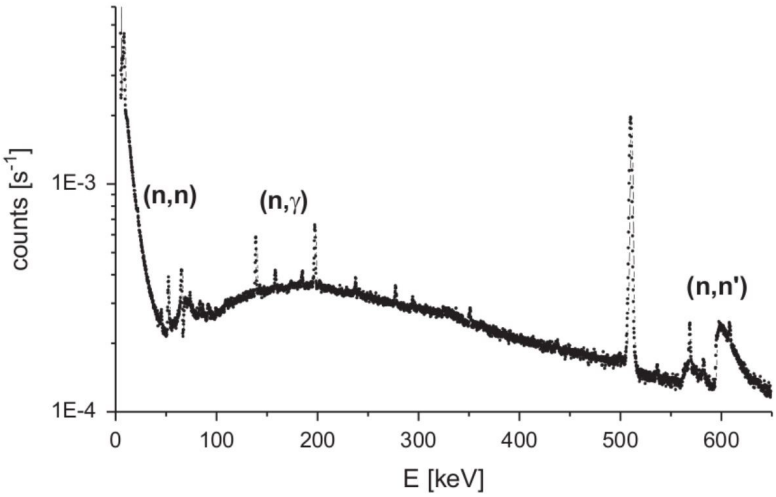

Figure 26: Characteristic gamma ray spectrum including the influence of neutron interactions [28].

A more detailed analysis of the background contribution from muons is postponed until a muon veto is set up. From experience with other detector set ups, a reduction of the muon background by a factor of ∼100 can be expected with an appropriate muon veto.

4.4 Background due to impurities in the lead shielding

Besides the radiation originating from the environment or from cosmic rays, one has to consider the background contribution from impurities in the lead, which will be used in the shielding of the Adam detector. While the other background components can be reduced significantly by proper shielding, the impurities in the lead are an unavoidable background source. Because of that, special selected lead is used which has a low contamination of impurities. For the lead close to the detector a block (20 cm x 20 cm x 13 cm) with a round hole and a low contamination of ^{210}Pb will be used. The lead block in discussion has an activity of 2.5 Bq/kg [26] and a mass of 50.6 kg. In this section, the influence of the impurities (^{210}Pb & ^{210}Bi) in this lead block is investigated.
The lead block was implemented in the software model and the decay of the two isotopes in the lead was simulated. Thereby, no lead was in the line of sight to the borehole, so direct radiation into the borehole was not possible. In the case of ^{210}Pb no signal was registered in the simulation, which is due to the low energetic gammas or betas, respectively, not being able to penetrate the end cap ($\frac{1}{e}$ attenuation after ~ 0.45 mm for a 50 keV gamma ray in monel [5]). The simulated spectrum for ^{210}Bi is shown in Fig. 27 for the low energy range. The previously discussed peaks in the background measurement (∼76 keV & ∼86 keV) are present as well.

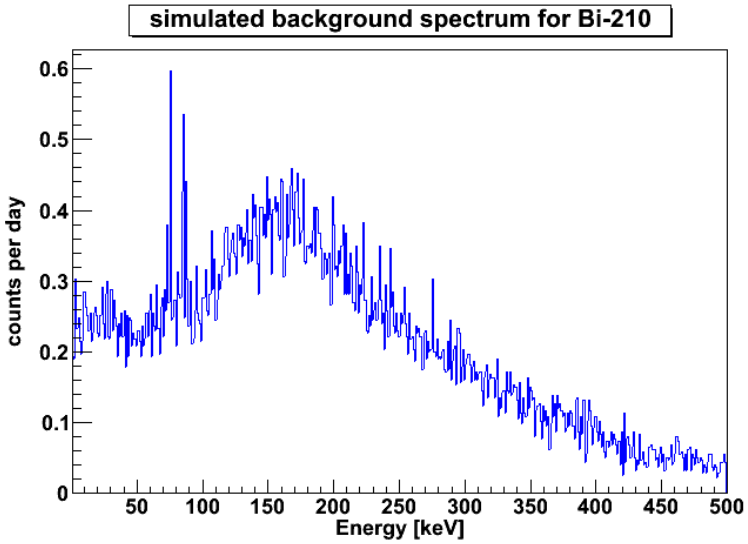

Figure 27: Simulated background spectrum in the low energy range originating from impurities in the lead shield.

In comparison, the overall count rate in the background spectrum (Fig. 23) is significantly higher, which is mainly due to the natural radioactivity in the environment. But one also has to consider that the lead in the provisional shield has a higher contamination of impurities than the block for the planned shielding, which was not used for the background measurement. Moreover, the simulation accounted only for the discussed lead block while the detector was surrounded completely by lead during the measurement. In contrast to the simulation radiation into the borehole was therefore possible during the measurement.
The simulation of the ^{210}Bi in the lead block is an estimate of the background contribution induced by the impurities in the lead. It represents the lowest background which can be achieved with additional shielding (muon veto, etc.). The lead, which is not close to the detector has more impurities, but the radiation emitted by it has less influence due to the self-absorption of lead. Moreover, the lead in front of the borehole will also contribute to the background, which is not considered in this estimate.

5 Simulation & Measurement of a ^{210}Pb source

The initial reason for setting-up the detector was the measurement of the 46.5 keV gamma ray line of ^{210}Pb. The decay of the radon daughter is a significant background component of the XENON1T experiment (wall leakage) [29]. The Adam detector will be used to test components for depositions of ^{210}Pb and to evaluate possible cleaning procedures to reduce the background. In order to probe if the detector is sensitive for this energy range, ^{210}Pb & ^{210}Bi were simulated to decay in a lead block filling the whole bore hole. The resulting spectrum is shown in Fig. 28.

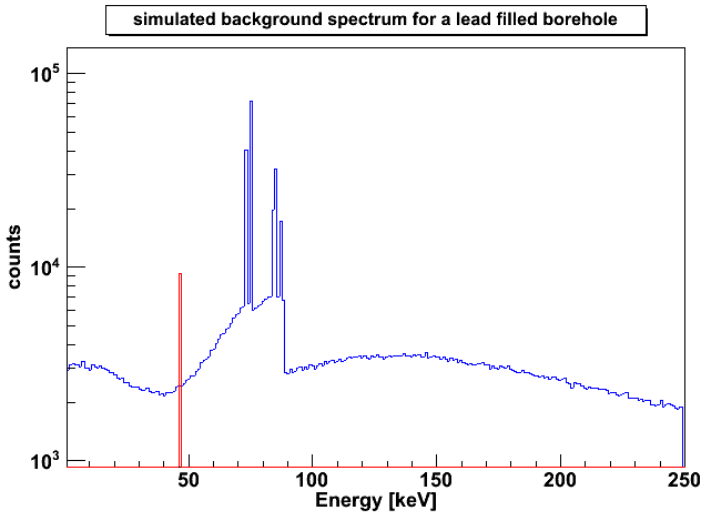

Figure 28: Simulated spectrum for ^{210}Pb (red) & ^{210}Bi (blue) started from a lead block filling the borehole completly. Each time 30 Mio. events were started.

The simulation shows that the detector should indeed be able to detect the 46.5 keV gamma line of ^{210}Pb. It is also apparent that the decay of ^{210}Bi by the same decay chain contributes significantly to the background of the desired 46.5 keV gamma line. In addition, ^{210}Bi induces lines between 70 keV & 90 keV, which have a significantly higher amplitude than the gamma from ^{210}Pb.
In a next step, an uncalibrated ^{210}Pb source was measured to test the detector in the intended low energy range. The point source was placed in front of the borehole since it was too big to fit into the borehole. The measurement in the low energy range is shown in Fig. 29, while Fig. 30 shows the region of interest of the 46.5 keV gamma line. A measurement with a calibrated low energy source was not possible since a suitable source was not available.

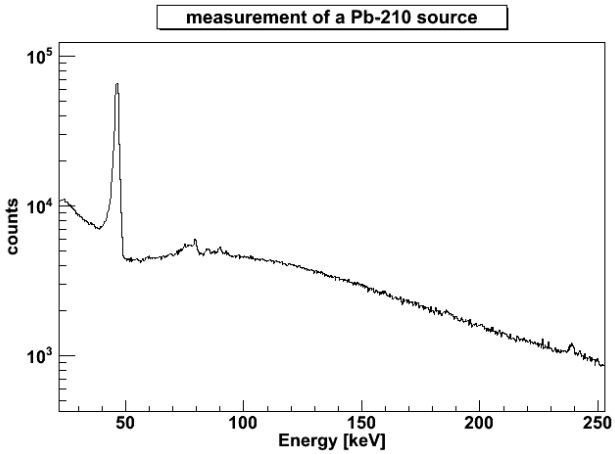

Figure 29: Measured spectrum of the Pb-source in the low energy range.

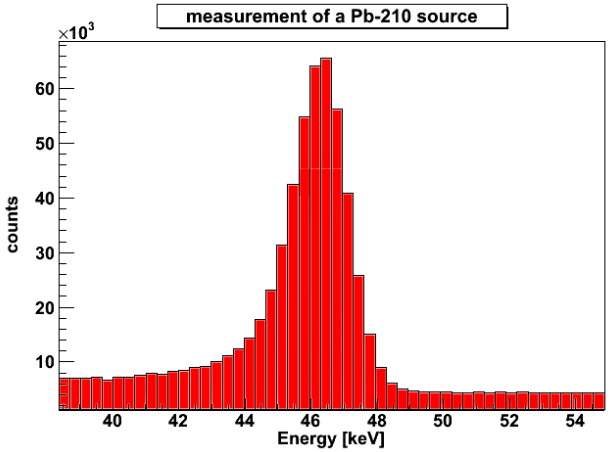

Figure 30: Measured spectrum of the Pb-source in the ROI of the 46.5 keV gamma line.

6 Results & Discussion

In this thesis the coax well gamma spectrometer Adam was characterized and implemented into a software model, which is crucial for later data analysis. Characteristic quantities such as the dead layer thickness and the thickness of the end cap were determined by matching the simulation to the measurement.
An averaged value for the dead layer thickness at the crystal mantle was obtained. It was apparent that the dead layer at the top was significantly thinner than elsewhere. It is possible that unknown parts inside the detector, e.g. the holding clamps, were influencing the measurement on the top. More measurements with varying positions along the detector axis are appropriate to investigate this deviation. This is also supported by the more detailed sketch in Fig. A.1. It could have been possible that the top measurment was pointed to the thinner part of the holding cup, which explains the measurement of a less thick dead layer. Since the samples are inserted into the borehole and the dead layer thickness at the mantle does not influence the measurement, the average value is sufficient for the software model.
The obtained results of the end cap thickness inside the borehole are in agreements with the values of contemporary well detectors. Future measurements along the borehole axis could confirm the homogeneity along the detector axis.
The implemented software model was then used to estimate the different background contributions and their expected reduction due to dedicated shielding. The background investigation should be continued while the different shielding components are set-up.
Finally, it was probed by a simulation and by a measurment if the detector is sensitive for the low energy range. A measurement with a calibrated source fitting into the borehole is required to further validate the software model.

7 Outlook

The work in this thesis was the first step for the reinstallation of the Adam detector. To have a fully functioning low level gamma spectrometer more preparations, such as a complete shielding, are necessary. The planned set-up for the Adam detector is shown in Fig. 31 and Fig. 32 which was made by the construction office at the MPIK.
The detector will have a lead shield completely surrounding it. Every line of sight pointing to the crystal from the outside will have at least 20 cm lead in between. As mentioned before, the lead which will be used close to the detector will have a low contamination of radioactive impurities. Around this lead layer, an air tight stainless steel chamber is going to be installed. The chamber will be flushed with nitrogen to remove the air which is contaminated with radon. Around the outer lead shield, each side besides the bottom will be covered by a muon veto. The muon veto consists of $\sim$5 cm thick scintillator plates with photo multiplier tubes connected to an anti-coincidence circuit. This set-up will pause the data acquisition when a muon

is hitting the detector.
For accessing the borehole and inserting samples four lead blocks of cylindrical shape can be removed. For sliding a teflon layer will be wrapped around them. The air tight stainless steel chamber will be sealed with an elastomer O-ring and multiple screws. The muon veto plate at the front will be opened by a sliding door. Furthermore, the detector is supposed to get a new DAQ system. After installation of the discussed shielding system and further optimization of the set-up, the detector can be put into operation. For each construction step the software model will be updated.

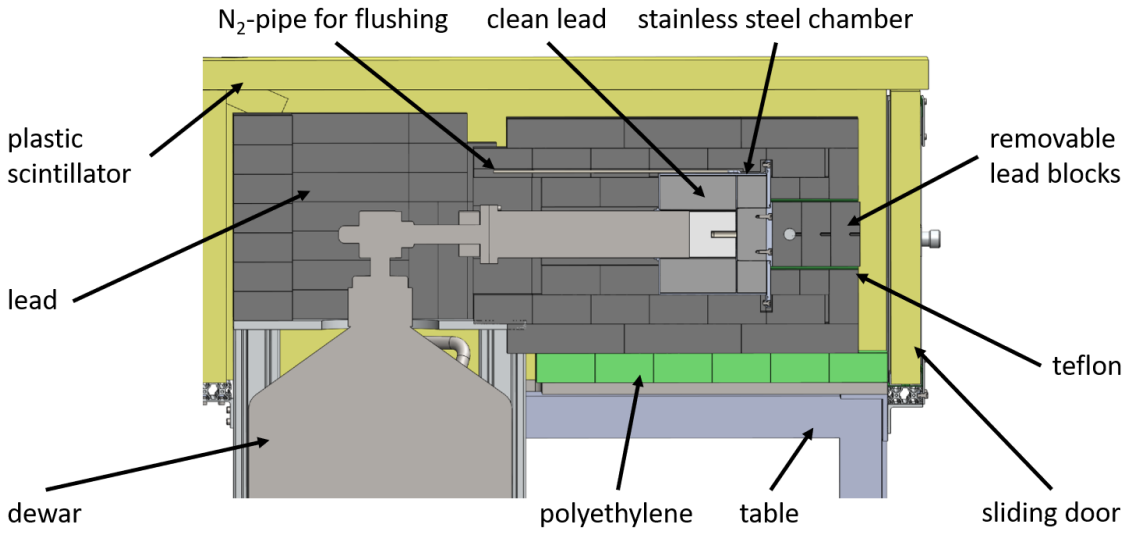

Figure 31: Planned set up for the Adam detector, side view [30].

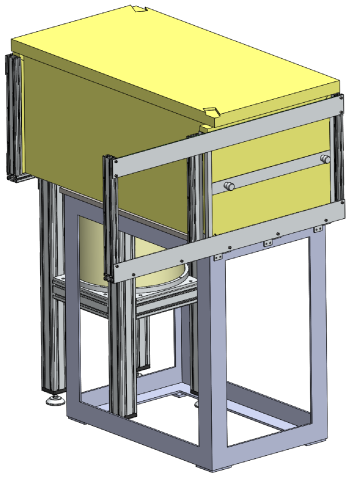

Figure 32: Planned shielding for the Adam detector [30]

Appendix

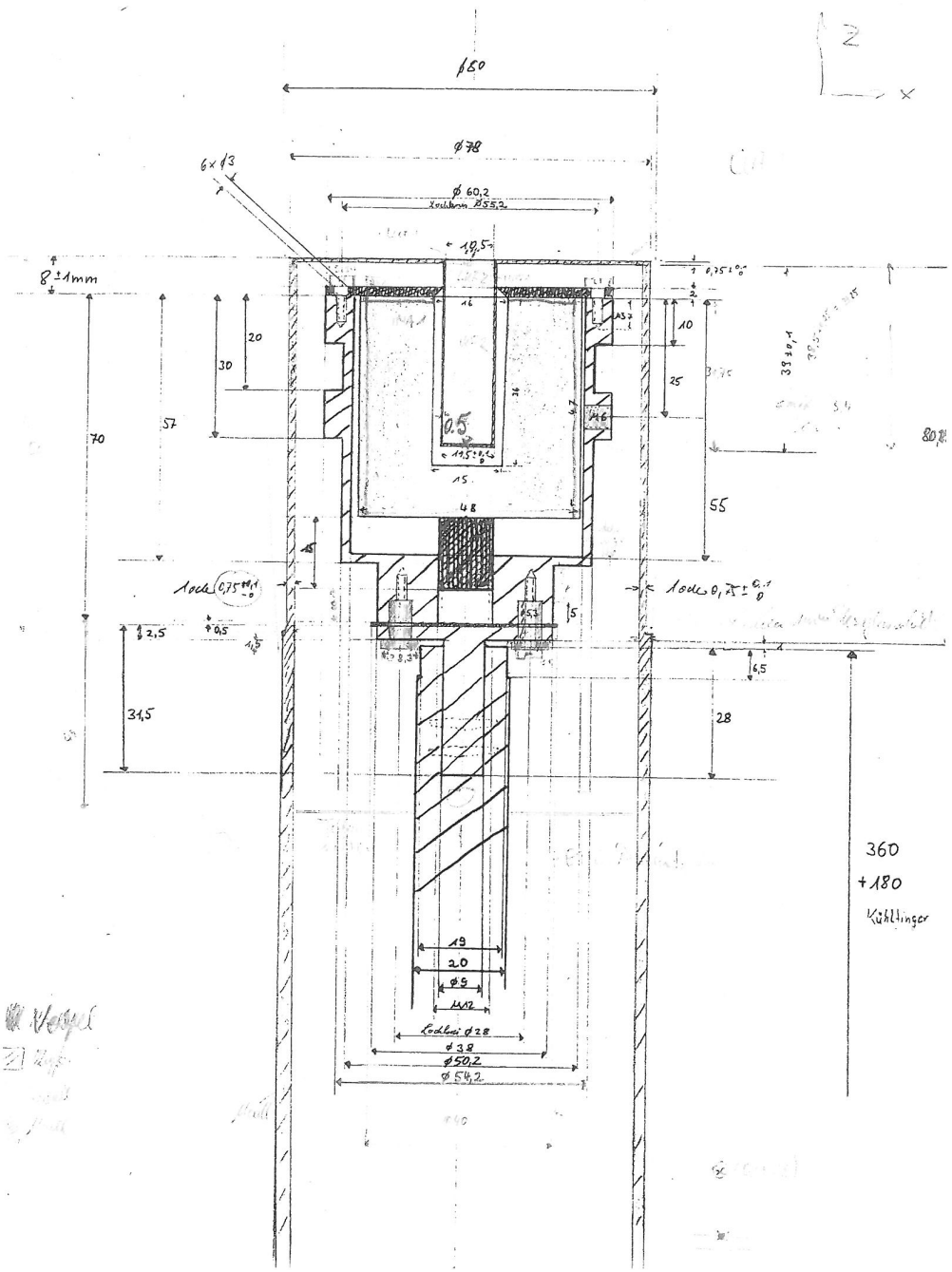

Figure A.1: Sketch of the Adam detector, showing the thickness of the end cap and the internal structure including the mounting of the crystal.

References

[1] E. Aprile et. al., "The XENON1T Dark Matter Experiment", *European Physics Journal* **2017**, *77*.

[2] M. Agostini et. al., "Measurement of the half-life of the two-neutrino double beta decay of ^{76}Ge with the GERDA experiment", *Journal of Physics G: Nuclear and Particle Physics* **2013**, *40*.

[3] G. Gilmore, J. Hemingway, *Practical Gamma-Ray Spectrometry*, John Wiley & Sons, **1995**.

[4] W.R. Leo, *Techniques for Nuclear and Particle Physics Experiments*, Springer Verlag, **1987**.

[5] National Institute of Standards and Technology, X-Ray Mass Attenuation Coefficients, `https://physics.nist.gov/PhysRefData/XrayMassCoef/tab3.html`, accessed: 12.07.2018.

[6] Dusan Budjas, *Germanium detector studies in the framework of the GERDA experiment*, **2009**.

[7] M. Ali Omar, *Elementary Solid State Physics*, Addison-Wesley, **1975**.

[8] P. Horowitz et. al., *The Art of electronics*, Cambridge University Press, **1989**.

[9] Chapter 8 Hyper-Pure Germanium Detector, `www.science.mcmaster.ca/radgrad/images/6R06CourseResources/4RA34RB3_Lecture_Note-8_HPGe_Detector.pdf`, accessed: 06.08.2018.

[10] Mark Heisel, *Low-Level γ-Spektrometrie an vers. Materialien für GERDA*, **2006**.

[11] G. Heusser, "Low Radioactivity Background Techniques", *Annual Review of Nuclear and Particle Science* **1995**, *45*, 543–590.

[12] Janina Hakenmüller, *Simulation of the cosmic ray induced background in the GIOVE detector*, **2015**.

[13] G. Heusser, "Cosmic ray-induced background in Ge-spectrometry", *Nuclear Instruments and Methods in Physics Research* **1993**, *83*, 223–228.

[14] creationwiki.org, decay chains, `http://creationwiki.org/File:DecayUranium-238-lead.png`, accessed: 09.08.2018.

[15] Werner Maneschg, *Low-Level-Gammaspektroskopie im Rahmen des GERDA-Experiments zur Suche nach dem neutrinolosen Doppel-Betazerfall in ^{76}Ge*, **2007**.

[16] G. Heusser et al., "GIOVE: a new detector setup for high sensitivity germanium spectroscopy at shallow depth", *The European Physical Journal C* **2015**.

[17] M. v. Sivers et al., "The GeMSE Facility for Low-Background γ-Ray Spectrometry", *Journal of Instrumentation* **2016**.

[18] G. Heusser et al., "Low-level germanium gamma-ray spectrometry at the μBq/kg level and future developments towards higher sensitivity".

[19] K. Weise et al., "Bayesian Decision Threshold, Detection Limit and Confidence Limits in Ionizing-Radiation Measurement", *Radiation Protection Dosimetry* **2006**.

[20] radiochemistry.org, Tl-208 Decay Scheme, `https://www.radiochemistry.org/periodictable/gamma_spectra/pdf/tl208.pdf`, accessed: 21.08.2018.

[21] Laboratoire National Henri Becquerel, Atomic and Nuclear data, `http://www.lnhb.fr/nuclear-data/nuclear-data-table/`, accessed: 09.07.2018.

[22] Canberra Industries, Canberra HPGe Detectors, `http://www.canberra.com/products/detectors/germanium-detectors.asp`, accessed: 07.07.2018.

[23] M. Boswell et al., "MaGe- a Geant4-based Monte Carlo application framewrok for low-background germanium experiments", *IEEE Trans. Nucl. Sci.* **2011**, *58*, 1212–1220.

[24] T. Skwarnicki, *A study of the radiative CASCADE transitions between the Upsilon-Prime and Upsilon resonances*, DESY F31-86-02, **1986**.

[25] University of Zurich, Absorption of γ-rays - Determination of the Half-value Thickness of Absorber Materials, `http://www.physik.uzh.ch/~matthias/espace-assistant/manuals/en/anleitung-ab_e.pdf`, accessed: 18.07.2018.

[26] Janina Hakenmüller, personal communication, **6.2018**.

[27] J. Nikolov et al., "Applicability of the Ge(n,γ) reaction for estimating thermal neutron flux", *Physics Procedia* **2014**, *59*, 71–77.

[28] M. Krmar et al., "A method to estimate a contribution of Ge(n,n') reaction to the low energy part of gamma spectra of HPGe detectors", *Nuclear Instruments and Methods in Physics Research* **2013**, *709*, 8–11.

[29] E. Aprile et al., "First Dark Matter Search Results from XENON1T Experiment", *Physical Review Letters* **2017**, *119*.

[30] Bettina Mörk (MPIK), construction plan of the planned Adam shield, **6.2018**.

Acknowledgments

Für die Möglichkeit meine Bachelorarbeit am Max-Planck-Institut für Kernphysik schreiben zu können, möchte ich mich bei allen Beteiligten, insbesondere Herrn Professor Dr. Dr. Manfred Lindner, bedanken.
Zudem danke ich Herrn Professor Dr. Wolfgang Hampel für seine Bereitschaft, die Zweitkorrektur meiner Arbeit zu übernehmen.
Des Weiteren möchte ich mich bei allen Beteiligten für die Teilnahme und insbesondere für deren Hilfe bei der Sensitivitätsanalyse bedanken.
Ein besonderes Anliegen ist es mir, mich bei meinem Betreuerteam Herrn Dr. Hardy Simgen und Herrn Dr. Stefan Brünner für Ihre vielfältige Unterstützung zu bedanken. Großer Dank gilt dabei Stefan für das mehrmalige Korrekturlesen und die hilfreichen Verbesserungsvorschläge.

Erklärung:

Ich versichere, dass ich diese Arbeit selbstständig verfasst habe und keine anderen als die angegebenen Quellen und Hilfsmittel benutzt habe.

Heidelberg, den 24.08.2018 .....